

Energetics and cathode voltages of LiMPO_4 olivines ($M = \text{Fe}, \text{Mn}$) from extended Hubbard functionals

Matteo Cococcioni* and Nicola Marzari

*Theory and Simulation of Materials (THEOS), and National Centre for Computational Design and Discovery of Novel Materials (MARVEL),
École Polytechnique Fédérale de Lausanne (EPFL), CH-1015 Lausanne, Switzerland*



(Received 5 November 2018; published 7 March 2019)

Transition-metal compounds pose serious challenges to first-principles calculations based on density-functional theory (DFT), due to the inability of most approximate exchange-correlation functionals to capture the localization of valence electrons on their d states, essential for a predictive modeling of their properties. In this work we focus on two representatives of a well known family of cathode materials for Li-ion batteries, namely the orthorhombic LiMPO_4 olivines ($M = \text{Fe}, \text{Mn}$). We show that extended Hubbard functionals with on-site (U) and intersite (V) interactions (so called DFT+ U + V) can predict the electronic structure of the mixed-valence phases, the formation energy of the materials with intermediate Li contents, and the overall average voltage of the battery with remarkable accuracy. We find, in particular, that the inclusion of intersite interactions in the corrective Hamiltonian improves considerably the prediction of thermodynamic quantities when electronic localization occurs in the presence of significant interatomic hybridization (as is the case for the Mn compound), and that the self-consistent evaluation of the effective interaction parameters as material- and ground-state-dependent quantities allows the prediction of energy differences between different phases and concentrations.

DOI: [10.1103/PhysRevMaterials.3.033801](https://doi.org/10.1103/PhysRevMaterials.3.033801)

I. INTRODUCTION

The search for new and more performant materials for Li-ion batteries has received a strong impulse in the last decade, first due to the development and diffusion of portable electronics and now also with a major focus on transportation and energy storage. These applications impose multiple requirements on the materials: of being lightweight, environmentally friendly, of having high gravimetric/volumetric energy density, high power, fast rechargeability, long life, thermal/chemical stability, and low fabrication costs. Despite steady progress in recent years and the introduction of new types of rechargeable batteries (e.g., K-, Na-, Mg-ion [1–4], or Li-air ones [5,6]) for dedicated purposes, many microscopic aspects of their behavior still need full clarification, with space for improvement and optimization [7–11]; significant research activity is taking place, in fact, on all battery components (anodes, cathodes, electrolytes) [12–14]. The constant efforts to improve performance have stimulated a vigorous search for better materials, especially for electrolytes (in the attempt to design solid-state media able to sustain safely higher voltages than their liquid counterparts, and comparable ionic currents) [15–22] and for cathodes (in order to identify more conductive, safer systems with higher energy density, higher voltage) [10,23–34]. Cathode materials are, in fact, particularly important for the improvement of rechargeable Li-ion batteries as these components are not only the source of power, but also embody some of the most critical bottlenecks

towards the improvement of current technologies including weight, safety, energy density, and overall power.

The relevance of the electronic and ionic degrees of freedom within the single particles or grains of the electrodes, and their role in determining the performance of Li-ion batteries (e.g., rate capability, energy density), has made the use of first-principles calculations fundamental in the understanding of their functionality and increasingly more common for the characterization and design of battery materials [28,35–54]. Since the open-circuit voltage corresponds to the redox potential of the electrochemically active species changing their oxidation state during the charge/discharge of the battery (these are often transition-metal ions), it is crucial for the energetics of various phases and compositions involved in the charge/discharge processes to be predicted accurately and reliably. High predictive accuracy is also needed for other quantities besides the voltage and the stability of the different phases appearing at intermediate Li concentrations, such as the formation energies of defects, or the viability of different doping strategies. A key difficulty in being quantitatively accurate in these predictions comes from the presence of transition-metal (TM) ions, typically present in variable oxidation states. In fact, most approximate exchange-correlation functionals used in current implementations of density-functional theory (DFT) [55,56], such as the local-density approximation (LDA) or the generalized-gradient approximation (GGA), tend to overstabilize delocalized states and are unable to capture accurately the localization of d electrons as a result of the remnant self-interaction errors present in functionals. Often these errors lead to a distinct failure in describing the ground state of materials at intermediate Li concentrations, predicting a metallic band structure and

*Present address: Department of Physics, University of Pavia, Via Bassi 6, 27100 Pavia, Italy.

an even distribution of electronic charge on TM ions, rather than the correct mixed-valence ground state, with electrons localized on a subgroup of TM ions at a lower oxidation state. This overstabilization of the metallic state typically compromises the reliability of total energies and the thermodynamics between different phases. For these reasons DFT calculations on these materials require functionals that are able to reduce or eliminate the spurious self-interaction that affects most of current approximations, to deliver a more pronounced localization on TM ions, and a faithful representation of mixed-valence ground states. Unfortunately, these requirements are very difficult to satisfy for functionals of the electronic charge density alone; even the recently introduced SCAN semilocal meta-GGA density functional [57], while very promising for various systems including layered oxides [58] and materials with well localized exchange-correlation holes [59], is not fully satisfactory for general systems affected by the above-mentioned problems, especially intermetallic transition-metal compounds [60,61]. The partial removal of the electronic self-interaction by adding a fraction of Fock exchange, as in hybrid functionals, greatly improves the localization of electrons [62] (albeit at a significant computational cost), but might not solve problematic aspects related to energetics, as reported in Ref. [63] and detailed below.

One meaningful alternative to correct for self-interaction errors is the DFT + Hubbard approach, where the exchange-correlation functional is augmented by a Hubbard-model Hamiltonian acting on localized states [64–72] (see in particular Refs. [73,74] for a discussion of self-interaction and DFT+ U). This approach was first applied to the study of cathode materials by some of us [75–77]; this work showed that DFT+ U with effective interactions computed from first-principles [78], albeit averaged over different Li contents, can promote a more pronounced localization of d electrons and predict average voltages (with respect to Li/Li⁺) in closer agreement with available experimental data, while also recovering the correct thermodynamics between phases. This effort led to Hubbard-corrected DFT becoming a standard computational tool to perform predictive first-principles calculations on Li-ion cathode materials, and over the last decade its use on these systems has been broad and successful [40,42,79–87]. Although the accuracy of the original application of DFT+ U to these materials was largely due to the possibility to compute the Hubbard parameter U from first principles, its semiempirical evaluation was often preferred, probably due to the complexity to evaluate U reliably and efficiently on every system of interest. Recent computational studies on cathode materials conducted with various flavors of DFT+ U have also reiterated some key characteristics or shortcomings [88,89], including (i) its dependence on its environment (structural, magnetic, and electronic phases); (ii) the impossibility to use material-dependent U 's in energy comparisons; (iii) the variation of U in proximity of defects (e.g., impurities, local deformations of the lattice, surfaces, etc); (iv) the difficulty to obtain a uniform improvement in the prediction of several properties with the same value of the Hubbard U [90]; and (v) the scarce reliability of DFT+ U in the presence of significant hybridization between the metal cations and the neighbor anions. To circumvent these issues hybrid functionals have become an increasingly popular choice for calculations

[62,91–93]. Although more computationally demanding, these functionals offer the advantage of containing at most one adjustable parameter, namely the fraction of exact (Fock) exchange, typically determined semiempirically [94] and held constant for all the systems analyzed. However, the overall quality of results obtained when using hybrid functionals turns out to be often comparable to those obtained with DFT+ U or approximate DFT functionals [62,95] with also some major qualitative failures, such as predicting a negative formation energy for Li_{0.5}FePO₄ [63], as mentioned earlier. We also underscore that in the vision outlined in Refs. [73,78] point (i) above is actually an intrinsic feature of DFT+ U ; in addition U should always be considered pseudopotential dependent, since it depends on the atomic Hubbard manifold on which it acts and this is influenced very significantly, e.g., by the oxidation state of the atomic all-electron reference calculation (see the Appendix of Ref. [74]).

The present paper studies in detail a well known class of cathode materials—Li-metal phosphates with the olivine (orthorhombic) structure—with the aim of addressing some of the methodological issues outlined above. These compounds, whose chemical formula is Li _{x} MPO₄ ($M = \text{Fe, Mn}$ in this work, with x varying between 0 and 1 during the discharge of the battery), represent a particularly appealing family for Li-ion batteries cathodes [96]. In fact, the presence of stable PO₄ tetrahedra as structural linkers improves the chemical stability of the cathode, reducing the chance of oxygen releases, and guarantees higher levels of safety for the device, especially if compared to that offered by other materials, such as LiCoO₂. Among the olivine phosphates LiFePO₄ is of primary technological interest (in fact, it is already largely used in the fabrication of commercial batteries) and is the object of intense research activity that aims at understanding its electronic properties and the surprisingly high (and still somewhat controversial) charge/discharge rate that nanostructured cathodes are able to sustain [41,50,97–104], despite its low ionic and electronic bulk conductivities. Ongoing research efforts are also targeting, at a more explorative level, other compounds of this family [105], with the main aim of improving the specific energy through higher voltages. While experiments assessing the performance of many of these compounds as cathode materials are made difficult by the unavailability of electrolytes able to sustain voltages higher than 3.5–4 V, there still remain many aspects of their behavior to be clarified, especially related to the occurrence and stability of other phases at intermediate Li content. Therefore, first-principles calculations aiming at a precise assessment of the energetics, from which the average voltage can be estimated [106], and of possible intermediate phases, represent a particularly precious tool for the characterization of these materials and for the assessment of their performance. As mentioned, this work will focus on two different olivine phosphates that have, respectively, Fe or Mn as transition-metal cations. In particular, it will aim at determining the equilibrium structure of these materials, the average voltage with respect to the Li/Li⁺ couple of a pure Li anode, the relative stability, and the formation energy of compounds with different Li contents ($x = 0, 0.5, 1$). Total energy calculations will be performed with an extended Hubbard-corrected functional (named DFT+ U + V) that contains both on-site (U) and intersite (V) effective electronic interactions

[107]. The work will clearly show the benefits of an improved description (thanks to the intersite term V) of the hybridization between transition-metal ions and their oxygen ligands to capture electronic localization and mixed-valence ground states. The presented results will also highlight the critical importance to compute (specifically, from linear-response theory (LRT) calculations in supercells [78]) the Hubbard interaction parameters in full consistency with the electronic ground state and the crystal structure of the materials considered in order to achieve quantitatively reliable energetics.

The remainder of the paper is structured as follows. Section II is devoted to describing the extended DFT+ U + V functional and to discussing the self-consistent linear-response procedure adopted to compute the effective electronic interactions U and V . Section III presents the results obtained for each of the materials considered, comparing them with available experimental data (e.g., voltages, equilibrium crystal structures) and discussing the accuracy of different computational approaches. Finally, some conclusions are proposed, highlighting the most important results and the main merits of this extended Hubbard approach to study battery materials and to perform quantitatively predictive total energy calculations. In the Supplemental Material [108] the results presented in the paper are validated through a comparison with those obtained from slightly different Hubbard corrections specifically, with finite Hubbard U also on O p states, Hubbard parameters evaluated from linear-response calculations in larger supercells, or from a recent implementation of LRT in density-functional perturbation theory (DFPT) [109].

II. METHODOLOGY

A. The DFT+ U + V functional and the self-consistent evaluation of U and V

The DFT+ U + V method was introduced in Ref. [107] as a generalization of DFT+ U (in its simplest, rotationally invariant formulation introduced by Dudarev *et al.* [68]), and it is based on an extended Hubbard model [110–115] that contains both on-site (U) and intersite (V) electronic interactions. The total energy functional can be expressed as follows:

$$E_{\text{DFT}+U+V} = E_{\text{DFT}} + \sum_{I,\sigma} \frac{U^I}{2} \text{Tr}[\mathbf{n}^{I\sigma} (\mathbf{1} - \mathbf{n}^{I\sigma})] - \sum_{I,J,\sigma}^* \frac{V^{IJ}}{2} \text{Tr}[\mathbf{n}^{I\sigma} \mathbf{n}^{J\sigma}], \quad (1)$$

where the atomic Hubbard manifold occupation matrices, obtained from the projection of Kohn-Sham (KS) states on the atomic Hubbard manifold, have been generalized to allow for interatomic terms ($I \neq J$):

$$n_{m,m'}^{IJ\sigma} = \sum_{k,v} f_{kv}^\sigma \langle \psi_{kv}^\sigma | \phi_m^J \rangle \langle \phi_m^I | \psi_{kv}^\sigma \rangle. \quad (2)$$

In Eq. (1) σ labels the spin of electrons while the star “*” over the second summation is a reminder that, for each atom I , the sum runs only over neighboring atoms J within a certain shell. The symbol “Tr” indicates the trace of the matrix to which it is applied, while the $\mathbf{1}$ in the second term represents the unitary matrix. In Eq. (2) f_{kv}^σ are the occupations of the KS

states ψ_{kv}^σ , labeled by a k -point index k and by a band index v , while ϕ_m^I are atomic states of the atom I , labeled by the magnetic quantum number m . The present work only uses a finite intersite interaction V between the d states of TM ions and the p states of their oxygen neighbors. Based on the above definitions, we note that Eq. (1) can also be rewritten more concisely as

$$E_{\text{DFT}+U+V} = E_{\text{DFT}} + \sum_{\sigma} \text{Tr} \frac{\mathbf{W}}{2} [\mathbf{n}^\sigma (\mathbf{1} - \mathbf{n}^\sigma)], \quad (3)$$

where the “Tr” operator is now understood to act also on implicit site indexes and the interaction matrix \mathbf{W} is such that $W_{II} = U^I$ and $W_{IJ} = V^{IJ}$, $\forall I \neq J$.

In order to understand how this extended corrective functional modifies the electronic structure of a system, it is useful to study the action of the Hubbard additional potential on a specific KS state. The generalized KS Hamiltonian can be obtained from the functional derivative of Eq. (3) with respect to the complex conjugate of the KS state:

$$\begin{aligned} \frac{\delta E_{\text{DFT}+U+V}}{\delta (\psi_{kv}^\sigma)^*} &= V_{\text{DFT}+U+V} |\psi_{kv}^\sigma\rangle = V_{\text{DFT}} |\psi_{kv}^\sigma\rangle \\ &+ \sum_I \frac{U^I}{2} \sum_{m,m'} (\delta_{mm'} - 2n_{m'm}^{II\sigma}) |\phi_m^I\rangle \langle \phi_{m'}^I | \psi_{kv}^\sigma\rangle \\ &- \sum_{I,J}^* V^{IJ} \sum_{m,m'} n_{m'm}^{IJ\sigma} |\phi_m^I\rangle \langle \phi_{m'}^J | \psi_{kv}^\sigma\rangle. \end{aligned} \quad (4)$$

From the equation above it can be seen that while the on-site part of the potential discourages partial atomic occupations, stabilizing states that are either full or empty, the intersite term favors states having significant overlap with atomic states of neighboring atoms (thus contributing substantially to $n_{m'm}^{II\sigma}$ with $I \neq J$). Given this competition between the two types of interactions an accurate and consistent evaluation of both parameters is crucial. In our work this task is achieved by using the linear-response approach for the calculation of U , introduced in Ref. [78], and extending it to the calculation of V , as discussed in Ref. [116]. Within this approach the intersite interaction V can be obtained as the off-diagonal element of the interaction matrix of which U represents the diagonal part; this has already been shown to be accurate in a number of different cases, from ionic oxides and covalent semiconductors [107] to transition-metal complexes [117].

In order to fully capture the dependence of the effective interactions on the electronic and crystal structures, in the present work we adopt a self-consistent procedure for their calculation that is an evolution of the one introduced in Ref. [73] and, already discussed in Refs. [107] and [116], has been used in a number of other studies afterwards [118–122]. A similar self-consistent approach was introduced, independently, in Ref. [81], albeit with some differences that will be highlighted below. The rationale of this approach relies on the evaluation of U and V using linear-response theory from a DFT+ U + V ground state until self-consistency. In practice, starting from an initial choice of these parameters U_{in}^1 and V_{in}^1 (possibly equal to 0) a sequence of linear-response calculations is started in which the interactions obtained from the i th step are used to generate the DFT+ U + V ground state

of the next one: $U_{\text{in}}^{i+1} = U_{\text{out}}^i$, $V_{\text{in}}^{i+1} = V_{\text{out}}^i$ (mixing schemes between “input” and “output” can be adopted to improve convergence). The sequence is terminated when input and output values of the effective interactions coincide within a numerical threshold. In this work we also perform a structural optimization (of both cell parameters and atomic positions) in between two successive calculations of the interactions parameters, in order to guarantee full consistency of their values also with the crystal structure. Indicating the interaction parameters with the general symbol W ($W = \{U, V\}$), the self-consistent procedure can be summarized as follows:

$$\begin{aligned} W_{\text{in}}^1 &\rightarrow \text{SO}(W_{\text{in}}^1) \rightarrow \text{LR}(W_{\text{in}}^1) \rightarrow W_{\text{out}}^1 = W_{\text{in}}^2 \\ &\rightarrow \text{SO}(W_{\text{in}}^2) \rightarrow \text{LR}(W_{\text{in}}^2) \rightarrow W_{\text{out}}^2 = W_{\text{in}}^3 \dots \\ W_{\text{out}}^i &= W_{\text{in}}^{i+1} = W_{\text{in}}^i \quad \text{and} \quad \text{ES}(W_{\text{in}}^{i+1}) = \text{ES}(W_{\text{in}}^i), \end{aligned}$$

where “SO” stands for structural optimization and “ES” for equilibrium (crystal) structure. The sequence is terminated when also the equilibrium crystal structure is converged. This procedure, which evolves the effective interactions with the ground state of the system, allows us to treat them as material- and environment-specific quantities (rather than as parameters of the calculation, as in most literature on Hubbard corrections, often oblivious to the fact that Hubbard parameters need to be pseudopotential specific) and this is one of the key aspects that will be discussed in this work.

It is important to stress that the approach chosen for the self-consistent calculation of U 's and V 's is slightly different than that adopted in Ref. [81]: in fact, in the LRT calculations starting from a DFT+ U + V ground state, the potential deriving from the Hubbard functional is kept fixed (computing it on unperturbed atomic occupation matrices) to make sure that only the DFT part contributes to the second derivative that defines the effective interactions. This procedure makes the evaluation of U and V consistent with their definition as effective spurious curvatures of the DFT energy with respect to atomic occupations [78]. It is also consistent with the use of newly obtained values as a new guess for the next iteration, rather than as a correction to those of the previous step. A thorough comparative analysis of various self-consistent procedures for computing the Hubbard interaction parameters has been recently proposed in Ref. [123]. It is useful to remark that, since the Hubbard potential during the calculation of the Hubbard parameters is fixed, the present work (as well as that of Ref. [107]) is consistent with and gives the same result of method 2 of Ref. [123] (the U_{scf} mentioned here corresponds to $U^{(2)}$ of that work). In fact, it can be proven that the Hubbard parameters calculated through the procedure just illustrated corresponds to the (atomically averaged) matrix element of the Hartree and exchange-correlation kernel, computed at the DFT+ U ground state with $U = U_{\text{in}}$.

For the sake of a precise numerical comparison of the Hubbard interaction parameters obtained, it would be appropriate to discuss screening of these quantities and how it is accounted for during their evaluation. This discussion is sketched in Ref. [124] presenting a linear-response calculation of the Hubbard parameters equivalent to (and based on) the one introduced in Ref. [78]. We remark here that the perturbation is screened by all the “other” electronic states, i.e., those that

are not explicitly perturbed by a shift in the potential acting on them. This implies that, in principle, the Hubbard U calculated for DFT+ U and DFT+ U + V ground states can be expected to be different from one another because the necessity to perturb neighbor ligand states for the evaluation of the intersite V leads, for the latter, to the removal of these states from the “screening” manifold. For most calculations presented in this work we decided to adopt a uniform strategy for computing the Hubbard interaction parameters and to always include the response of relevant ligand states (typically, O $2p$). The validity of this choice was then assessed for DFT+ U calculations on Li_xFePO_4 by comparing the values of U obtained as outlined above with those from calculations that did not include perturbations of O atoms. A further confirmation of the quality of this approximation is provided by the comparison with calculations of the Hubbard parameters based on DFPT [109], as is detailed in the Supplemental Material [108].

B. Formation energies and voltages

Most of the results presented in this work concern the evaluation of formation energies and (average) voltages, of which this section provides a definition.

Given a generic system S (able to reversibly intercalate Li ions in its structure) the formation energy of the compound Li_xS ($0 \leq x \leq 1$) with respect to the LiS and S component is evaluated as a weighted difference of total energies:

$$E_f(x) = E(\text{Li}_x\text{S}) - xE(\text{LiS}) - (1-x)E(\text{S}). \quad (5)$$

This formula is approximate at finite temperatures, where the difference between free energies (rather than total/internal energies) should be considered. While widely used in literature, the cancellation between the entropic terms seems a reasonable assumption for the vibrational part, while the configurational (e.g., ionic, electronic, magnetic) contributions to the entropy should, in principle, be handled with care. This is a particularly difficult task for intermediate Li concentrations. In fact, while for fully lithiated and delithiated compounds ($x = 0$ and $x = 1$) this only involves screening different spin configurations of the transition-metal ions, at fractional values of x additional important terms arise from the Li fractional occupation of available sites [125–128] and from the electronic “configurational entropy” related to the localization of valence d electrons on a subset of transition-metal ions. This latter term can in fact determine the stabilization of intermediate compounds, as previously discussed for Li_xFePO_4 [86].

In this work, following most of the literature on the topic, the evaluation of the stability of compounds at intermediate Li content will be based on total energies. A significant effort has been focused however on capturing the localization of electrons on transition-metal ions (i.e., the differentiation of these ions in subgroups of different valence) and on the quantitative comparison of different Li configurations at $x = 0.5$.

Another important quantity that can be evaluated from the direct comparison of total energies is the voltage (i.e., the Li intercalation potential) with respect to an ideal Li/Li⁺ anode. For a generic system S , considered as a cathode material, this quantity is in general a function of the Li content (although most valuable systems show no/very low dependence of the voltage on x , at least for a good part of the admissible range).

Its average value, between Li concentrations x_1 and x_2 ($x_2 > x_1$), can be computed as

$$\phi_{x_1, x_2} = -\frac{E(\text{Li}_{x_2}\text{S}) - E(\text{Li}_{x_1}\text{S}) - (x_2 - x_1)E(\text{Li})}{(x_2 - x_1)e}. \quad (6)$$

The total energies entering this formula are obviously referred to the same amount of material (e.g., one formula unit or one unit cell of the crystal) and $E(\text{Li})$ represents the total energy of an equivalent number of Li atoms in bulk Li (representing the anode), while e stands for the electronic charge. As noted for the calculation of formation energies and also for voltages, total energies should be replaced by total free energies; however, it is a common practice to compare voltages obtained from total energies with the results of experiments at finite T . The assumption of cancellation of the entropic terms in the difference between free energies is on firmer ground than in the evaluation of formation energies if voltages are computed across the whole range of variation of Li content, i.e., between $x_1 = 0$ and $x_2 = 1$, because then no calculation is needed at intermediate Li concentrations: for both the fully lithiated and delithiated compounds the configurational entropy due to either electrons or Li ions vanishes, while terms related to spin configurations, broadly independent from the Li content, presumably cancel. In this work we will adopt this common practice and will evaluate the average voltages balancing the total energies of fully lithiated and delithiated compounds. This quantity assumes a particularly simple expression that corresponds to the formation energy of the fully lithiated compounds (with respect to the delithiated one and bulk Li) normalized by the electronic charge:

$$\phi = -\frac{E(\text{LiS}) - E(\text{S}) - E(\text{Li})}{e}. \quad (7)$$

III. TECHNICAL DETAILS

The first-principles calculations presented in this work are all performed using the pseudopotential, plane-wave implementation of DFT contained in the Quantum ESPRESSO distribution [129,130]. In all cases a generalized-gradient approximation (GGA) functional is chosen, constructed with the PBEsol parametrization [131], particularly well suited for crystalline solids. In the calculations discussed in this work different systems were modeled with pseudopotentials of different types: the Fe olivine was described with ultrasoft pseudopotentials [132] taken from the Pslibrary 1.0.0 [133,134], while for the Mn compound PAW pseudopotentials [135] were taken from the Pslibrary 0.3.1 [136,137] following the Standard Solid State Pseudopotentials library (SSSP) validation protocols [138]. More detailed information about the pseudopotentials and the parameters used in the calculations are given in the sections dedicated to presenting results on specific systems.

The orthorhombic unit cell of the olivine materials considered in this work contains four formula units (24 to 28 atoms, depending on Li content), and is large enough to accommodate a few antiferromagnetic configurations (detailed and compared for selected compositions, see the following material-specific sections) and five Li concentrations (specifically, $x = 0, 0.25, 0.5, 0.75, 1$) of which $x = 0, 0.5, 1$ will be explicitly considered in this work. As an illustrative example,

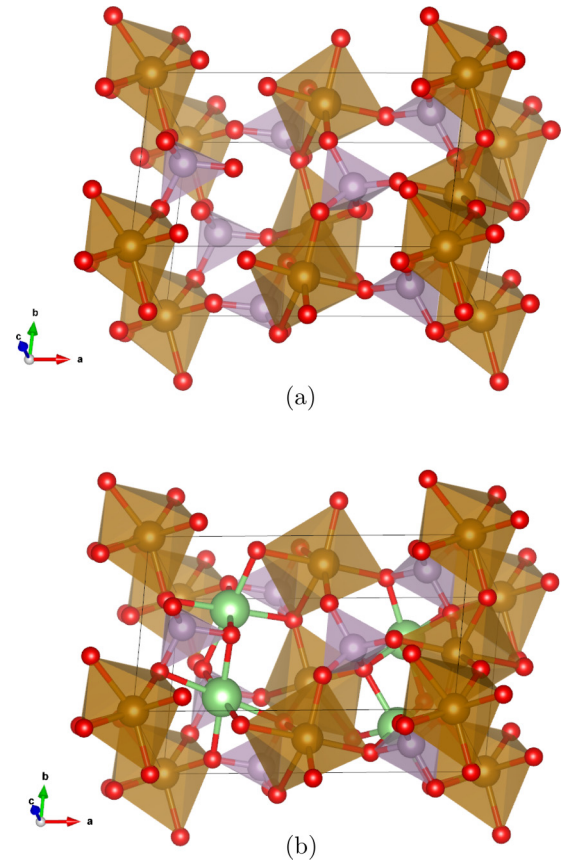


FIG. 1. The unit cell of FePO_4 (a) and LiFePO_4 (b). In evidence both the corner-sharing Fe-O octahedra and the P-O tetrahedra acting as linkers between them. The comparison between the two cells highlights the position of Li ions along channels parallel to the b axis of the orthorhombic cell.

Fig. 1 compares the $x = 0$ and $x = 1$ crystal structures (unit cells) of the Fe system. The unit cell of transition-metal phosphates is often attributed the $Pnma$ space group with the longest dimension along the x axis, and the y direction along the chain's Li ions form when fully occupying the available sites. As can be observed from Fig. 1, transition-metal ions are coordinated by six oxygen octahedra that are distorted from their ideal, cubic symmetry and tilted with respect to neighbor ones. TM-O octahedra are connected to each other either by sharing apical oxygens or by PO_4 tetrahedra which also share apical oxygens and act as structural linkers. This structural framework, which is the same also in the Mn phosphate, undergoes relatively minor but TM-dependent distortions upon Li insertion. This structural stability (together with the chemical one) is one of the main aspects that makes these crystals good cathode materials, as it enables the possibility to undergo several lithiation cycles with minimal structural damage. Given the proportions of the unit cell (roughly twice as long along a than along b and c), integrations over the Brillouin zone of this lattice were determined to require a $2 \times 4 \times 4$ grid of special k points [139] along with a Methfessel-Paxton [140] or Gaussian smearing of the Fermi occupation function of 10^{-2} Ry. Since the system has an insulating ground state, in principle it could be treated

within a fixed-occupations scheme. However, starting the self-consistent calculation of the Hubbard parameters from a DFT ground state, typically metallic, requires the use of a finite smearing of occupations that also facilitates, from a technical point of view, the description of magnetic systems.

The same four-formula-units supercell is also used to compute the Hubbard interaction parameters using the linear-response method introduced in [78]. For DFT+ U + V calculations the effective interactions of the Fe and Mn olivines are also computed in a $1 \times 2 \times 2$ supercell of the one described above, to study the convergence of the Hubbard interactions with the cell size. It is important to remark that, as already discussed in Ref. [107], computing V does not require any modification to the linear-response (LR) approach introduced in [78] (in fact, V is obtained as the off-diagonal element of the atomic interaction matrix); however, it implies perturbing also nontransition-metal states, which increases proportionally the cost of the LR calculations. In the present work, since calculations include intersite interactions between transition-metal ions and their first neighbors, oxygen atoms are also individually perturbed. More specifically, perturbations are imposed on the $3d$ states of transition-metal ions and on the $2p$ states of oxygens. While perturbing oxygens' p states is strictly necessary only for DFT+ U + V calculations, the procedure outlined above was adopted also for on-site-only DFT+ U calculations. A second series of calculation of the Hubbard parameters was performed for both the DFT+ U and DFT+ U + V cases, using a new implementation of the linear-response method based on density-functional perturbation theory (DFPT) [109]. As detailed in the Supplemental Material [108] this DFPT-based approach overall confirms (typically adding a slight quantitative refinement) the results discussed in the next sections, obtained from the smallest (four-formula units) cell, even if deviations of the computed values of the Hubbard parameters are occasionally observed.

As mentioned in the previous section, the interaction parameters of the corrective Hubbard functional are computed self-consistently with respect to both the electronic and crystal structures. It is worth keeping in mind that while DFT+ U + V total energy calculations (including the ones linear-response calculations are based on) are performed on an orthogonalized Hubbard basis, structural optimizations are performed without orthogonalizing it. This inconsistency, due to the technical difficulty of implementing forces and stresses from DFT+ U + V in an orthogonal atomic basis set, is expected to lead to marginal errors, and the crystal structures computed in this paper can be considered essentially identical to the full self-consistent ones. In any case this is common practice in all implementations of DFT+ U .

IV. RESULTS

A. Li_xFePO_4

1. *Electronic structure and energetics*

Among TM phosphates with the olivine (orthorhombic) structure, Li_xFePO_4 is currently the most widely used in commercial Li-ion batteries and certainly one of the most intensely studied in literature. In fact, after it was proposed as a potential cathode material in 1997 [96], due to its relatively high capacity, superior thermal, chemical, and mechanical

stability, low cost, and environmental friendliness of its components, this material has become the object of a fervent research activity aimed at improving the understanding of its properties and its behavior when employed in actual devices. While the use of nanostructured cathodes has allowed us to overcome the low ionic and electronic conductivities of this material (thus permitting its large-scale deployment in commercial devices), the microscopic diffusion mechanisms [39,40,46,48,103,141–147] and the nucleation, relative stability, and transformation dynamics of various phases [47,50,86,97–99,101,148–154] occurring during the charge and discharge transients of the battery are still a matter of intense research. In fact, in light of the very limited miscibility of Li-rich and Li-poor phases (somewhat increased at the nanoscale due to the higher free energy costs for the creation of interfaces [45,155,156]), the explanations of the relatively fast charge and discharge cycles observed in nanostructured cathodes is still quite controversial, as it is expected to involve out-of-equilibrium phenomena such as phase-transformation wave dynamics [104], metastable intermediate phases [97,99,149,151], or solid solutions [41,98,102]. This difficulty in interpreting the observed behavior constitutes a further motivation to precisely assess the energetics, the equilibrium crystal structure, and the relative stability of the material at different Li concentrations, which is the main scope of this work.

As mentioned in Sec. III, the transition-metal phosphates studied here are modeled with an orthorhombic 24-atoms unit cell (unless explicitly indicated) that corresponds to four formula units (see Fig. 1). This cell is large enough to accommodate a few antiferromagnetic states and Li configurations which will be compared in the last part of this section. While the energy scale of inter-atomic magnetic interactions makes the comparison of various AFM configurations marginally relevant for the energetics of the material (in particular, for its average voltage and the formation energy of the half-lithiated compound) especially at finite temperatures, this comparative analysis is still interesting to better understand the electronic structure of cathode materials [157] and, in general, to improve their characterization (in comparison with experiments) [158,159], especially if a significant shift of magnetic properties (e.g., the Néel temperature) is expected to correlate with Li intercalation. All the calculations shown in the first part are performed for the antiferromagnetic ordering (named AF1 in the later discussion) that was verified to correspond to the ground state configuration. The comparative evaluation of different phases of the partially lithiated system is, instead, more important to assess cathode performance. In fact, the mechanisms and kinetics of the (de)lithiation process during the charge and discharge transients are governed by how Li ions intercalate into the structure of the partially lithiated material. In spite of very limited miscibility, half-lithiated phases have been reported to form at the interface of the $x = 1$ and $x = 0$ regions [97,99,151], probably stabilized by the partial relaxation of the misfit stress that they allow, mediating the lattice mismatch between the two end phases [45,155]. While the topic is still controversial (the thickness and orientation of interfacial half-lithiated phases is observed to depend on the size of the particles [99,151] and possibly on the operational conditions [102]), assessing the relative

TABLE I. The values of U 's and V 's (in eV) for the three Li concentrations considered, computed within various flavors of Hubbard-corrected functionals. The ranges of values reported for the V parameters refer to different O ions in the first coordination shell, since values vary with the M-O distance. For $\text{Li}_{0.5}\text{FePO}_4$ the two sets of values refer to the Fe^{2+} and Fe^{3+} ions, respectively.

	Interaction	LiFePO_4	$\text{Li}_{0.5}\text{FePO}_4$	FePO_4
DFT+ U_{ave}	U_{Fe}		6.93	
DFT+ U	U_{Fe}	4.88	5.08/5.53	5.21
DFT+ $U+V$	U_{Fe}	5.14	5.44/5.05	5.30
	$V_{\text{Fe-O}}$	0.30–0.88	0.28–1.12/0.39–0.82	0.52–1.12

stability (i.e., the energy of formation) and comparing the crystal structures of crystals with intermediate Li content with those of the fully lithiated and delithiated compounds provides relevant information to evaluate the energy cost to form these interfaces, the magnitude of strains in their surrounding that might contribute to their stabilization, and the kinetics of Li ions inside the electrodes' bulk. In this work we will consider two specific half-lithiated crystals, both alternating fully occupied and unoccupied Li planes that are parallel to the yz plane in the first case, and to the xz plane in the second one. These structures will be called “ yz ” and “ xz ,” respectively. Since a full set of calculations with all the various flavors of Hubbard corrections was performed only for the first of the half-lithiated structures, the second will be considered only in the last part of the section, in the context of a quantitative comparison between the two.

The calculations on the Fe olivine were performed using an ultrasoft pseudopotential for Fe (with semicore $3s$ and $3p$ states in valence, along with $4s$ and $4p$) that required kinetic energy cutoffs of 85 and 650 Ry for the electronic wave functions and charge density, respectively. In this section we compare the results obtained within various approximations, all based on the same GGA (PBEsol) functional, which are labeled as GGA, DFT+ U_{ave} , DFT+ U , DFT+ $U+V$. For the sake of completeness, in Sec. S A of the Supplemental Material [108] we also present results obtained from DFT+ $U+V$ with a finite U on the p states of oxygen, with the Hubbard parameters computed from a larger $1 \times 2 \times 2$ supercell, or from DFPT (named, respectively, DFT+ $U^{dp}+V$, DFT+ $U+V_{1 \times 2 \times 2}$, DFT+ U_{DFPT} , and DFT+ $U+V_{\text{DFPT}}$). DFT+ U_{ave} and DFT+ U are both based on standard Hubbard corrective functionals [i.e., the first two terms in Eq. (1)]; however, the Hubbard U is computed in two different ways, one common in the literature, and one presented here. In DFT+ U_{ave} , GGA is used to optimize the structure at $x = 0, 0.5$, and 1. The Hubbard U is then computed from a single-shot LR calculation for each of these three crystals in their respective equilibrium configurations and averaged over them. The average value of the Hubbard U obtained in this way is then used to calculate the total energy of the crystal for the three Li concentrations and to evaluate the (average) voltage and the formation energy of the $x = 0.5$ compounds, without further optimization of the crystal structure. This is the common procedure followed in literature when the Hubbard U is computed from first principles rather than being determined semiempirically by fitting existing experimental data; for this reason the DFT+ U_{ave} results will be used as a benchmark with respect to those from the other corrective functionals used in this work. Instead, in DFT+ U

(and also in DFT+ $U+V$) the Hubbard interaction parameters are computed self-consistently (both with the electronic and crystal structures), according to the procedure described previously in Sec. II A. In particular, the intersite Hubbard interactions (V) are computed and used between Fe and nearest-neighbor oxygen ions. In these cases, no averaging is performed and all energy balances are obtained from calculations using material-specific and Li-concentration dependent U 's and V 's.

Table I shows the values of all the interaction parameters computed for each of the Li concentrations considered for the Fe olivine and for the flavors of the Hubbard corrective functionals outlined above. Additional results can be found in Table S.I. It is easy to note that the value of U obtained from a single-shot LR calculation on the GGA ground state (and averaged) is significantly higher than all the others, which is probably a consequence of the lack of consistency with the electronic ground state. Substantial differences between the self-consistent values of the Hubbard parameters can also be noted comparing the results at different Li concentrations (i.e., in dependence of the level of oxidation of the metal ion) or the results of different approaches when the same material or the same oxidation state of Fe are considered. For example, the value of V between $\text{Fe}^{2+} 3d$ and O $2p$ states changes depending on whether the Fe ion is one of LiFePO_4 or of $\text{Li}_{0.5}\text{FePO}_4$. Equally significant differences can in fact be noted comparing the values of U obtained for $\text{Li}_{0.5}\text{FePO}_4$ and FePO_4 within different flavours of the Hubbard correction or for Fe ions in the $x = 0.5$ compound and those in the same oxidation state in either fully lithiated or delithiated materials. These differences, which are the result of the self-consistent procedure adopted in the calculation of U 's and V 's, confirm a sensitivity of their values on the fine details of the chemical and crystal environments of the transition-metal ions they refer to, and suggest a limited portability of these parameters from one system to another, even when treated within the same approximations.

Based on these observations, we argue that the Hubbard interactions should not be considered as parameters of the calculation, nor should be thought of as simple functions of average quantities. We prefer instead to view these as quantities that depend on the electronic structure of the system, whose value is determined self-consistently by the ground state they contribute to determine. This point of view justifies our self-consistent calculation of the Hubbard interaction parameters, which is further supported by the overall agreement of the equilibrium crystal structure (Table II) with the experimental data for DFT+ $U+V$ and the significant improvement over DFT+ U obtained with the introduction of the intersite

TABLE II. The equilibrium lattice parameters (in bohr) of Li_xFePO_4 , $x = 0, 0.5, 1$, computed with DFT (GGA at the PBEsol level) and with the Hubbard $+U$ and $+U+V$ corrections, and compared with available experimental values (the superscripts a and b indicate Refs. [160] and [96], respectively).

		GGA	DFT+ U	DFT+ $U+V$	Expt.
LiFePO_4	a	19.31	19.57	19.52	$19.54^a/19.53^b$
	b/a	0.58	0.58	0.58	$0.58^{a,b}$
	c/a	0.46	0.45	0.45	$0.45^{a,b}$
$\text{Li}_{0.5}\text{FePO}_4$	a	18.87	18.92	19.08	
	b/a	0.59	0.59	0.59	
	c/a	0.48	0.48	0.47	
FePO_4	a	18.64	18.69	18.61	$18.44^a/18.56^b$
	b/a	0.59	0.59	0.59	$0.59^{a,b}$
	c/a	0.49	0.49	0.49	$0.49^{a,b}$

interaction V in the energetics and electronic structure (see later), in spite of the quite broad range of self-consistent values for U 's and V 's.

As apparent from Table II, the DFT+ U functional tends to expand the equilibrium lattice parameters with respect to those obtained from GGA calculations. The presence of intersite interactions partially counteracts this tendency, and mitigates the effect of the on-site effective repulsion U . For LiFePO_4 , compared to available experimental data of Refs. [96,160], GGA uncharacteristically underestimates the equilibrium lattice parameters while DFT+ U produces an optimized unit cell in quite good agreement with the data. This result is further refined by DFT+ $U+V$. Because of the experimental difficulties in stabilizing any compound at intermediate Li concentration, no measurement of the equilibrium lattice parameter of $\text{Li}_{0.5}\text{FePO}_4$ is, to the best of our knowledge, available. As for the $x = 1$ case, we can observe that DFT+ U leads to an expansion of the equilibrium lattice parameters compared to GGA. However, at variance with the fully lithiated case, the addition of the intersite interaction V yields a further expansion of the lattice. It is useful to mention that the unit cell of the $x = 0.5$ compound considered here undergoes a monoclinic distortion and the angle β between a and c decreases its amplitude from 90° to about 88° (the variations between different approaches are negligible). For FePO_4 , GGA equilibrium lattice parameters slightly overestimate (by less than 1%, in most cases) the experimental values. DFT+ U further expands lattice parameters with largest effects on the (longest) a axis. The addition of

the intersite coupling generally improves the prediction of the cell parameters over the GGA results and produces the best agreement with available experimental data.

The key results of this work for Li_xFePO_4 are displayed in Table III, which shows the total occupation of the d states for Fe ions [the trace of the diagonal blocks of the matrix defined in Eq. (2)], the formation energy of $\text{Li}_{0.5}\text{FePO}_4$, and the average voltage with respect to Li/Li^+ , computed as indicated in Eq. (6). Analyzing the atomic occupations it is evident how the GGA (PBEsol) functional fails to capture the charge disproportionation that should be observed upon delithiation and the consequent differentiation of Fe ions into 2+ and 3+. In fact, one should observe the occupations in the mixed-valence $\text{Fe}^{2+}/\text{Fe}^{3+}$ case mirroring those of the pure 2+ or 3+ cases. This failure results from the incomplete localization of valence electrons on the d states due to the defective cancellation of the electronic self-interaction, which is a well known problem of most approximate DFT functionals. DFT+ U is effective in fixing this problem [38–42,75–77] and, favoring integer occupations of atomic states, stabilizes a charge-disproportionated ground state thus leading to a clear distinction between 2+ and 3+ Fe ions. In fact, as evident from the DFT+ U_{ave} results in Table III, consistently with previous work, half of the Fe ions in $\text{Li}_{0.5}\text{FePO}_4$ have an occupation that closely resembles that of the (2+) Fe ions in LiFePO_4 , the other half that of the (3+) Fe ions in FePO_4 . When the Hubbard U is computed self-consistently, within DFT+ U , the roles of 2+ and 3+ are inverted: the 2+ Fe is not the one closest to the Li, as expected, but the one furthest apart. However, as it will be discussed later, this is a spurious result, probably a consequence of the system getting trapped in a local minimum of the energy. Using the extended corrective functional DFT+ $U+V$, the Fe ions closest to Li correctly recover their 2+ state.

The results shown in Table III are based on a Löwdin population analysis of Fe 3d states, according to the definition given in Eq. (2). That the numerical values are not in agreement with chemical practice (that would attribute six d electrons to Fe^{2+} and five to Fe^{3+}) is related to both the mathematical definition of the occupation matrices (not a univocal choice), to the physics of the system (e.g., some degree of hybridization between Fe 3d states and neighboring O 2p states), and, in general, to other reasons discussed in Refs. [161,162]. However, it is important to remark that our Hubbard corrections recover an electronic structure that is fully consistent with a charge-disproportionated state, with Fe^{2+} and Fe^{3+} ions described in full consistency with the end members of the Li_xFePO_4 system.

TABLE III. Löwdin total occupations of Fe 3d states, formation energy, and average voltage computed with different methods for Li_xFePO_4 , in comparison with available experimental data. It should be stressed how the mixed-valence occupations are described very accurately, in addition to the voltage.

	Fe^{2+} ($x = 1$)	$\text{Fe}^{2+}/\text{Fe}^{3+}$ ($x = 0.5$)	Fe^{3+} ($x = 0$)	F. E. (meV/f.u.)	Voltage (V)
GGA	6.33	6.11/6.08	5.93	-126	2.72
DFT+ U_{ave}	6.18	6.19/5.68	5.65	161	4.09
DFT+ U	6.20	5.74/6.19	5.71	191	3.83
DFT+ $U+V$	6.22	6.22/5.77	5.76	107	3.51
Expt.				>0	~3.5

Regarding the formation energy of the $x = 0.5$ compound, the GGA calculations return a negative value that contradicts the lack of observation of stable phases at $x = 0.5$. These results confirm the conclusions of previous work [75] that already showed how this situation is due to the overstabilization of the incorrect metallic state obtained at intermediate Li content (both the $x = 0$ and $x = 1$ materials are predicted to be insulators) which lowers the total energy of the $x = 0.5$ compound compared to the weighted average of the fully lithiated and delithiated end points. The incomplete localization of valence electrons is also at the origin of the significant underestimation (-0.8 V) of the voltage: in fact, this quantity can be broadly related to the energy made available to the system by each Fe ion when it is reduced from a 3+ to a 2+ oxidation state. By promoting the localization of valence d electrons DFT+ U reverts this tendency and produces a positive formation energy for $x = 0.5$ and a voltage in much better agreement with the experimental value. However, the best results are obtained when the intersite V between Fe $3d$ and O $2p$ states is switched on, leading to a predicted voltage which is less than 0.1 V off from the experimental value. In comparison, hybrid functionals, while improving electron localization and charge disproportionation, generally result in average voltages of comparable quality [62], but do not systematically improve errors on formation energies [63]. In order to better understand the effects on the ground-state electronic structure of the various electronic interactions, we compare in Fig. 2 the density of states (DOS) for the fully lithiated material, obtained with the approximations discussed above. All graphs reported in the figure show the total DOS (black dashed line) with the total contributions from the transition-metal d states (solid red lines for majority spin, green for minority) and from (spin-unpolarized) oxygen p states. As evident from the figure, while the GGA (PBEsol) functional predicts a metallic behavior with the Fermi level of the system crossing the minority-spin d states, DFT+ U is effective in opening a band gap (of about 4.5 eV if the average value of U is used) in the Kohn-Sham spectrum of the material by separating a single occupied minority-spin d state from the rest of its manifold (Fe²⁺ has nominally six d electrons and in its highest spin configuration has five electrons in one spin state and the remaining one in the other). DFT+ U + V also predicts an insulating ground state; however the band gap is lower (≈ 4 eV) than in DFT+ U and closer to the experimental value (≈ 3.7 eV). Another notable difference from the on-site only DFT+ U is that the occupied minority-spin d state shows a lower contribution in the energy window dominated by oxygen p states and majority-spin d states, while it dominates the energy window at the top of the valence manifold with a strong peak.

On a more technical level, it is fair to remark that the DFT+ U_{ave} and the DFT+ U results presented above can be expected to be slightly less accurate than the others, since the Hubbard U were obtained including the response of oxygen ions into the susceptibility matrices. As mentioned at the end of Sec. II A, this can lead to the underscreening of the effective interaction parameter that results from the linear-response calculations. In order to precisely assess the entity of this approximation DFT+ U_{ave} calculations were repeated for Li _{x} FePO₄ with a Hubbard U computed from a linear-response

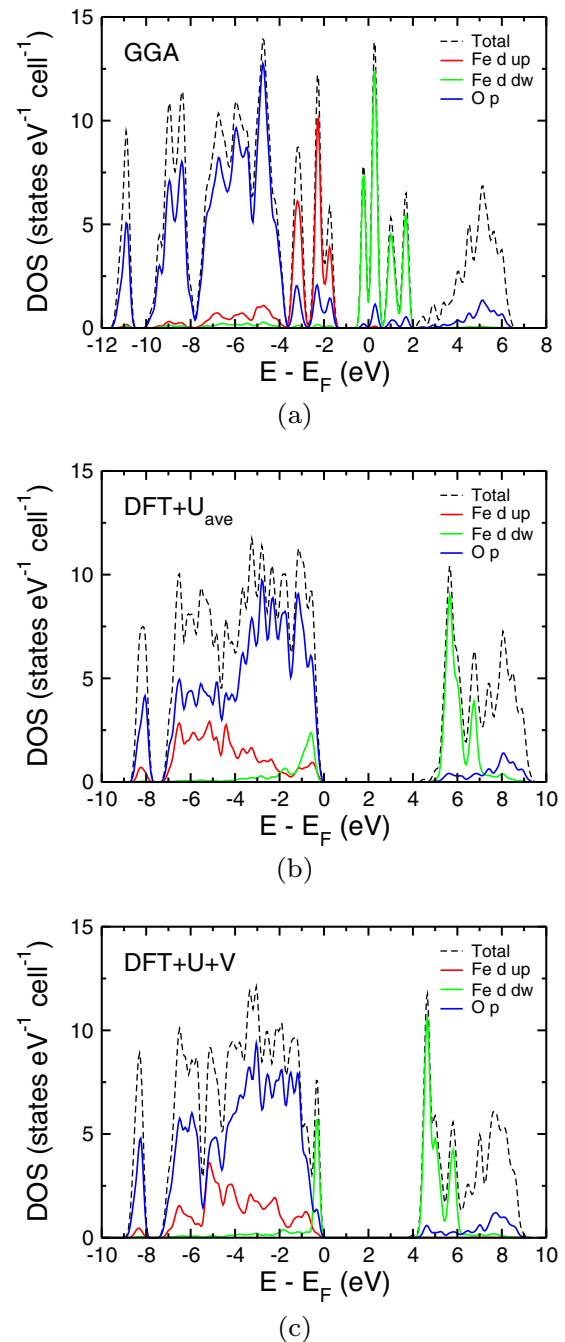


FIG. 2. The density of states of LiFePO₄ obtained with different approximations: (a) GGA (PBEsol), (b) DFT+ U_{ave} , and (c) DFT+ U + V . In all the graphs the black dashed line represents the total density of state while solid red, green, and blue ones designate iron d state spin up, iron d state spin down, and oxygen p states total contributions, respectively. All energies are referred to the Fermi level or to the top of the valence band in the presence of a gap.

procedure that only involved perturbing Fe ions. The value of the Hubbard U obtained this way (after averaging over the results of the three calculations at $x = 0, 0.5$, and 1), is 6.25 eV which, due to the additional screening from the oxygen p states, is more than 0.5 eV lower than the one computed previously (see Table I). In spite of this significant difference in the numerical value of the effective parameter, however,

TABLE IV. The magnetic moments arrangements for the Fe ions in LiFePO_4 for all four configurations compared in this paper. The coordinates of the Fe ions are given in crystalline units and correspond to the equilibrium structure obtained with $\text{DFT}+U+V$. ΔE represents the energy differences (in meV per formula unit) between them as obtained from the $\text{DFT}+U+V$ energy (see text for details), when PBEsol is used.

	a	b	c	AF ₁	AF ₂	AF ₃	FM
Fe ₁	0.00	0.00	0.00	↑	↑	↑	↑
Fe ₂	0.50	0.00	0.55	↑	↓	↓	↑
Fe ₃	0.94	0.50	0.50	↓	↓	↑	↑
Fe ₄	0.44	0.50	0.05	↓	↑	↓	↑
ΔE				0.0	3.1	12.1	16.1

the values of the formation energy of the $x = 0.5$ compound and of the average voltage are 159 meV per formula unit and 3.96 V, respectively, which are very close with those reported in Table III. These quantities thus seem to be robust with respect to the amount of screening included in the calculation of the effective Hubbard parameters (although a more precise assessment should also take into account the optimization of the crystal structure). The same conclusions are corroborated by a further validation of the results presented so far that was obtained by recomputing (self-consistently) the effective Hubbard parameters from DFPT [109]. The details of these results are presented in the Supplemental Material [108]. An important outcome of these calculations is that the better control offered by DFPT on the convergence of the Hubbard parameters and the lower numerical noise they are affected by in smaller cells, might help avoiding local minima (actually relatively common with Hubbard corrected functionals) along the self-consistent calculation of interactions, electronic and crystal structures, as the one found within $\text{DFT}+U$ for $\text{Li}_{0.5}\text{FePO}_4$, and leading to the swapping of 2^+ and 3^+ Fe ions.

2. Li ion and magnetic configurations

After a thorough discussion and a quantitative analysis of the results of various Hubbard corrections a comparison is now performed between different possible configurations of the magnetic moments localized on the Fe ions and between two Li orderings already introduced at the beginning of this section, alternating full and empty Li planes parallel, respectively, to the yz and the xz crystallographic planes. These comparative analyses will be aimed at establishing the most energetically favorable configurations and at assessing, through the evaluation of energy differences, the possibility for the system to visit higher energy (metastable) configurations, e.g., under the nonequilibrium conditions it experiences during the charge/discharge transients of the battery, especially in high currents regimes [41,97,102].

The comparison between different magnetic configurations is performed only for the fully lithiated material (LiFePO_4); however, similar conclusions are obtained also for FePO_4 and can presumably be extended to all Li concentrations. Table IV provides a scheme illustrating the relative orientation of the magnetic moments on Fe ions (identified by their crystalline coordinates) in the three antiferromagnetic and the ferromag-

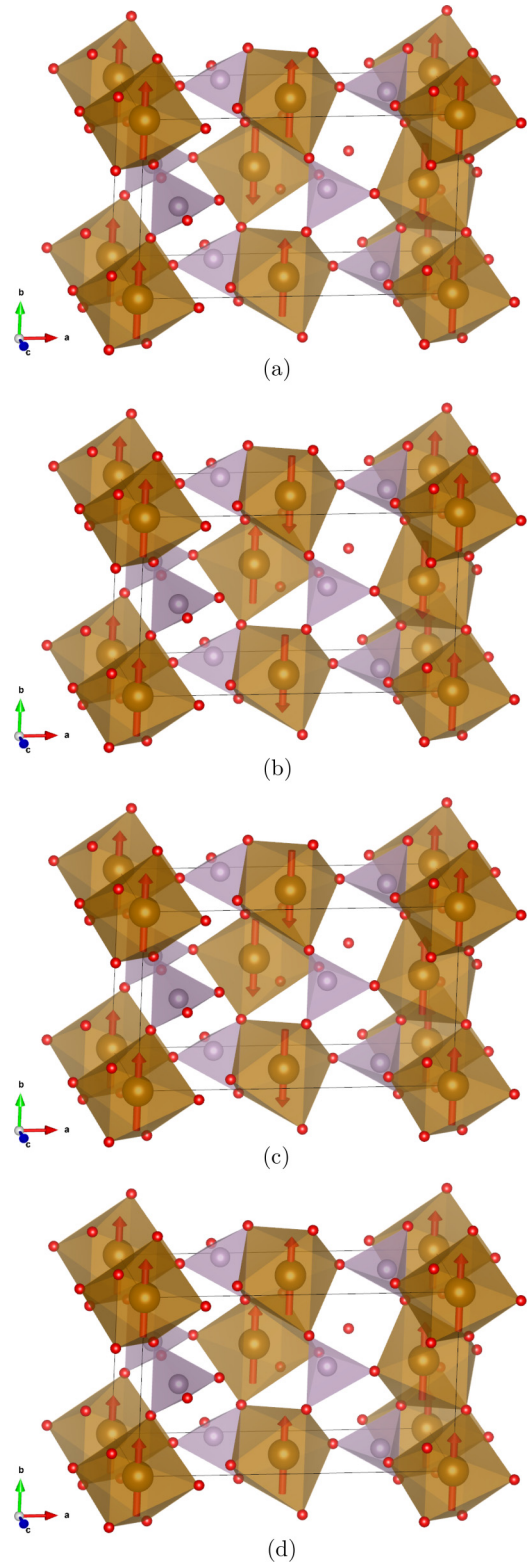


FIG. 3. The four magnetic configurations of LiFePO_4 compared in the text: (a) AF₁, (b) AF₂, (c) AF₃, and (d) FM. Note that the Li atoms have been removed from the figures to improve clarity.

netic configurations, compatible with the primitive (28-atoms) unit cell of the crystal. In its last row it also compares their energies as obtained from $\text{DFT}+U+V$ calculations. The comparison is further eased by Fig. 3 which offers a visual repre-

sentation of the unit cell for the $x = 1$ material (although Li ions were removed from the picture) in the four configurations considered. The arrows on the Fe ions indicate their magnetic moments. Since all calculations were performed with a collinear spin functional and with no spin-orbit coupling, the direction of the magnetic moments of the Fe ions is arbitrary and the arrows in the figure point in a generic direction. In the first configuration (AF_1) the antiferromagnetic ground state is realized by ferromagnetic (010) planes alternating with opposite magnetization. This spacial distribution of magnetic moments implies that when Fe-O octahedra share one vertex oxygen their magnetization is antiparallel; conversely, their moments are parallel if they are connected through a P-O tetrahedron. In the second configuration (AF_2), instead, each Fe has a magnetic momentum antiparallel to that of all its first neighbors, independently from how their octahedra are connected. Finally, the third antiferromagnetic configuration (AF_3) consists of ferromagnetic (100) planes alternating with opposite magnetization. As reported in Table IV, total energies of the various magnetic configurations are ordered as follows: $E_{AF1} < E_{AF2} < E_{AF3} < E_{FM}$. This ordering is consistent with previous work in literature [157,160] (at least for the ground and first-excited states) and is robust with respect the particular approximation being used, although the energy differences between the various magnetic orders varies with the specific flavor of Hubbard correction in use. For example, for the PBEsol functional the energies of AF_2 and AF_3 are about 10.8 and 19.3 meV/f.u. higher than that of AF_1 , respectively. The antiferromagnetic configuration that results as the ground state is the same adopted in the first part of this section for all three Li concentrations considered. The comparison between various magnetic orders presented here thus provides an *a posteriori* justification for adopting it in the first place. Relaxing the crystal structures turned out, in all cases, irrelevant for the ordering reported above (the reported energies are the ones obtained from the optimized structures in all cases) and, in many cases, changed very little the energy splittings between the various phases. This result was obtained without adapting self-consistently the U and V interaction parameters and maintaining their value equal to that of the ground state AF_1 . However, based on the relatively minor changes in the crystal structure and on the weak dependence of the atomic charge on the relative spin arrangement, this approximation is expected to be quite good. A further point in support of this procedure is the relative numerical irrelevance of the intersite Fe-Fe terms of the response matrices (which are expected to be affected the most by a change in the relative spin orientation) in determining the values of U 's and V 's. In summary, independently from the functional adopted for the calculation and the particular flavor of Hubbard correction, the energy difference between different magnetic configurations is very small and largely irrelevant (in fact, one order of magnitude smaller) for the evaluation of important quantities such as formation energies and average voltages.

A second important comparative analysis is now developed between two Li configurations for the half-lithiated $Li_{0.5}FePO_4$ material, shown in Fig. 4. The first of them [Fig. 4(a)], with Li occupying alternate yz planes (thus named “ yz ” here) has been proposed to be forming in the surrounding of the interface between the $x = 0$ and $x = 1$ regions in

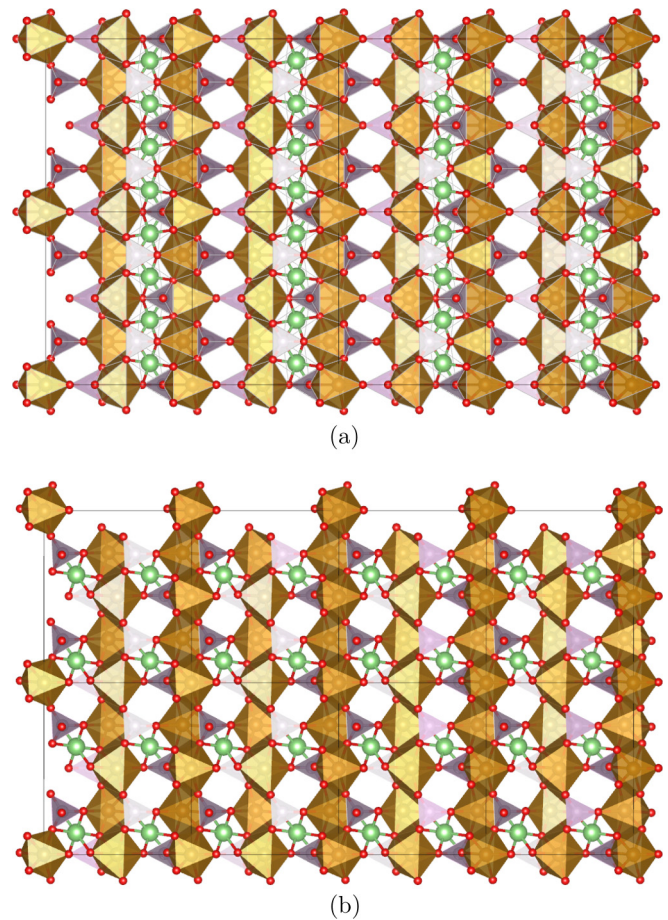


FIG. 4. The two Li configurations considered for $Li_{0.5}FePO_4$ with Li occupying alternate yz (a) and xz (b) planes. The two supercells present a view of the crystal along the $[001]$ direction.

small particles of the partially lithiated system, during the charge/discharge transients [at least at low (de)lithiation rates] or after they have reached the equilibrium configuration (the observed samples were obtained by disassembling a half-charged battery, cycled at low rates) [99,151]. According to these works this intermediate $x = 0.5$ phase is stabilized by the relaxation of the interfacial stress between lithiated and delithiated regions (due to a milder lattice mismatch) until the energetic cost of its formation offsets the gain in elastic energy. The relaxation of interfacial elastic energy is also corroborated by the observation that the thickness of this half-lithiated layer depends inversely on the size of the particle [99]. A previous computational study on this intermediate phase has highlighted instead its role in enhancing the motion of the above-mentioned interfaces during the charge and discharge of the battery through a significant reduction (compared to a sharp interface) of the kinetic barriers Li has to overcome during its diffusion throughout the material [50]. The second of these half-lithiated phases, with Li occupying alternate xz planes (and named “ xz ”), has been proposed to be one of the intermediate configurations the system visits when the (de)lithiation process, at high charge/discharge rates (high overpotentials and currents), proceeds through nonequilibrium solid solutions of progressively lower/higher Li content

[41,102]. This mechanism is expected to be viable even at relatively low temperatures due to the low formation energy of a plethora of partially lithiated phases with respect to the end members. Based on the results presented previously, our comparative analysis on these crystals is based on DFT+ U + V calculations only, with U and V evaluated self-consistently with both the electronic and crystal structures as explained in Sec. III, for both configurations. The main result of our calculations concerns the total energy of the two $x = 0.5$ phases. We obtain the second phase to be lower in energy than the first by about 65 meV per formula unit and, with a formation energy of 42.5 meV per formula unit, it results in being relatively more accessible for a system at finite temperatures. While significantly lower than that of the yz configuration, this formation energy is however somewhat higher than that reported in Refs. [41,102], obtained from Monte Carlo simulations. It is interesting to note that the different position of Li ions also induces a redistribution of valence electrons on the transition-metal ions; in particular, between the two configurations, the Fe ions swap their oxidation state (the ones that are in a 2+ state in the first become 3+ in the second, and vice versa). Consistently with chemical intuition and with the localized nature of d electrons, the Fe ions that are closer to the Li result in both cases in the 2+ oxidation state, thus confirming that Li motion correlates with the diffusion of localized electronic charges in their neighborhood. As highlighted previously, this correlation between the position of Li ions and electrons is quite hard to capture with approximate exchange-correlation functionals, especially for the second configuration in which the difference between the Fe-Li distances for the 2+ and 3+ ions is significantly smaller. The use of the extended Hubbard correction, with a consistent calculation of the interaction parameters, produces instead a consistent description of the two valence states of Fe ions (both categories of Fe ions having practically the same atomic occupation in the two configurations) while polarizing the crystal structure around Fe ions consistently with their valence. It is interesting to note that also the Hubbard U 's assume values that are consistent between the two Li configurations for ions in the same oxidation state, with those for the second structure resulting in values of U of 4.96 and 4.86 eV for the 3+ and 2+ Fe ions, respectively, in excellent agreement with those shown in Table I. The values of the intersite interaction parameters, instead, do not show the same agreement between the two configurations (those for the second structure result in the 0.19–0.54 eV and 0.15–0.59 eV ranges for the 3+ and 2+ ions, respectively), probably reflecting a different distortion of the oxygen octahedra coordinating the Fe centers.

B. Li_xMnPO_4

1. Electronic structure and energetics

The potential of Li_xMnPO_4 (LMPO) as a possible cathode material for Li-ion batteries was already recognized in the seminal work by Padhi *et al.* [96] which first promoted phospho-olivines as positive electrode materials. Compared to the isostructural LFPO, LMPO presents a higher voltage (4.1 V vs Li/Li⁺) which is quite an appealing feature in perspective of its use in higher energy density cathodes, still within the breakdown potential of most liquid electrolytes

currently available. Unfortunately, LMPO is also plagued by several problems that have so far prevented its deployment in actual devices. Among these, particularly harmful are a lower chemical stability (especially of the delithiated phase) that makes the material prone to parasitic reactions with consequent rapid loss of capacity; possibly less safe and more difficult to synthesize using the same techniques successful for LFPO [163–165]; a larger volume/lattice mismatch between lithiated and delithiated phases that increases the chances of permanent structural defects at interfaces and makes the material lose its cyclability more rapidly [166,167]; a difficult deposition of C on the surface of nanostructured LMPO samples, needed to improve their electronic conductivity [164,168,169]; the Jahn-Teller (JT) activity of Mn³⁺ ions (in the delithiated phase), promoting quite significant structural distortions in their local environment (in particular of the oxygen cage around them), and abrupt changes also in the electronic structure that may impact negatively the performance of the material. The most serious problem for using LMPO in actual devices is represented, however, by its low ionic and electronic conductivities that, while further compromised by passivation events during the charge and discharge of the battery or by lattice disorder (with Mn²⁺ ions possibly obstructing the Li diffusion channels) [167], are generally attributed to the significant lattice polarization around injected charges (leading to the formation of polarons) that are caused or enhanced by the JT activity of Mn³⁺ ions and result in sluggish motion of the charge carriers (i.e., high effective masses or higher kinetic barriers for the hopping to neighbor sites) [63,170]. The necessity to find a way around these problems and to define viable strategies to employ LMPO in actual cathodes of Li batteries has stimulated a quite lively research activity on this material (summarized, e.g., in Ref. [165]) that has encompassed the precise characterization of its structural, magnetic, and electrochemical properties [170,171], but also the development of new fabrication techniques that could improve its performance as cathode material [167–169,172–175]. Several computational studies have also been performed on this system, generally focusing on the electronic, magnetic, structural, and vibrational properties of LMPO [176]. A particular attention in this context has been devoted to the study of the local distortion around the (possibly JT-active) 3+ Mn ions and to its impact on the ionic and electronic conductivities [166,177], occasionally addressed quantitatively through the evaluation of relevant kinetic barriers [63].

In this work a computational study of this material is presented that focuses on ground state electronic, magnetic, and structural properties. The same Li concentrations examined for LFPO are also considered for LFMO and for each of them a ground state consistent with the choice of the Hubbard flavor and the value of the interaction parameters is computed. A similar comparative analysis between the three materials is also performed discussing the crystal structures (with a particular focus on the local environment of Mn ions), the number of electrons on their d orbitals (directly related to their oxidation state), and the total energies. The latter will be employed for the calculation of the formation energy of the $x = 0.5$ system and of the average voltage vs Li/Li⁺. Because of the role played by the hybridization between Mn and O in determining the local distortion of the crystal and its transport properties,

TABLE V. The values of U 's and V 's (in eV) obtained for Li_xMnPO_4 , $x = 0, 0.5, 1$, computed within various flavors of the Hubbard correction (see text). The ranges of values reported for the V parameters refer to the first coordination shell (their values vary with the M-O distance). For $\text{Li}_{0.5}\text{MnPO}_4$ the two sets of values refer to the 2+ and 3+ Mn ions, respectively.

		LiMnPO_4	$\text{Li}_{0.5}\text{MnPO}_4$	MnPO_4
DFT+ U_{ave}	U_{Mn}		5.66	
DFT+ U	U_{Mn}	5.28	7.48/8.28	8.20
DFT+ $U+V$	U_{Mn}	4.44	4.96/6.27	6.28
	$V_{\text{Mn-O}}$	0.55–1.20	0.24–1.62/0.52–1.26	0.56–1.39

LMPO will represent a particularly significant test case for the extended Hubbard functional discussed in this work and will highlight the importance of the intersite interactions to capture the properties of systems where valence electrons do not completely localize on atomic states. As in the case of LFPO, also for this system a comparative analysis is performed between various antiferromagnetic configurations of the $x = 1$ compound and between different possible ordered phases of the half-lithiated material. Given the similarity between the two systems, the same Li and magnetic configurations of the Fe-based material are considered. The results are discussed in the last part of this section, while its first part concerns the AF1 configuration and the $x = 0.5$ structure with Li filling alternating yz planes.

As mentioned in Sec. III, the computational study on this system was performed using a PAW pseudopotential [135] which also included Mn $3s$ and $3p$ states into the valence manifold. These calculations required kinetic energy cutoffs of 100 and 400 Ry for the plane-wave expansion of the electronic wave functions and charge density, respectively. Brillouin zone integrations were performed using the same $2 \times 4 \times 4$ special k -point grid also adopted for LFPO.

Table V reports the values of the effective U 's and V 's obtained for the Li_xMnPO_4 system ($x = 0, 0.5, 1$) using the self-consistent linear-response approach discussed in Sec. II A. Similarly to the case of LFPO even in this case the values of the Hubbard parameters referring to Mn ions in the same oxidation state can change quite significantly with Li content, especially for 2+ Mn ions. At the same time, the effective interactions change their values also in dependence of the specific Hubbard functional adopted in their self-consistent evaluation. For example, the value of U varies quite significantly depending on whether the intersite V is used in the total energy calculations or not, and on whether structural relaxations are involved in the procedure. As in the case of LFPO, the value of Hubbard parameters vary quite significantly with the oxidation state. It is important to remark that the different values of U and V for the 2+ and 3+ ions in the half-lithiated material were obtained as a result of the linear-response approach discussed in Sec. II A. Their differentiation was not enforced in any way, although it is certainly the effect of a different crystal environment around 2+ and 3+ sites. All these observations confirm the scarce portability of the Hubbard parameters and the necessity to compute them consistently for the system of interest and with the same approximate functional (exchange-correlation and Hubbard correction) that is used in the calculations.

Table VI allows us to compare the equilibrium crystal structure obtained for this system within various

approximations. In general, given the overall agreement on b/a and c/a , it is possible to ascribe the mismatch with the experimental results to an almost uniform linear scale factor. For the fully lithiated compound GGA slightly underestimates (up to about 2%) the lattice parameters with respect to their experimental value. The self-consistent DFT+ U overcorrects this tendency resulting in equilibrium cell axes that are longer than predicted by experiments. When the intersite interaction is turned on the general agreement between the computed and the experimental crystal structure is significantly improved with differences that are within a fraction percent for all the structural parameters. The same trends just discussed for $x = 1$ can be observed for the half-lithiated and delithiated compounds, with DFT+ $U+V$ correcting the expansion of the unit cell stabilized when only the on-site U is used and predicting values for the lattice parameters that are intermediate between GGA and DFT+ U . However, for $x = 0$ the best agreement with experimental results is obtained from GGA (slightly overestimating lattice parameters), while DFT+ $U+V$ shows a mismatch with the experimental cell parameters in the 2%–3% range. This result, at variance with what was obtained for FPO (see Table II), is somewhat surprising in light of the overall improvement obtained with DFT+ $U+V$ on the electronic structure and energetics (average voltage) of the material (see below). The half-lithiated compound, modeled by the same “staged” arrangement of Li atoms also used for

TABLE VI. The equilibrium lattice parameters (in bohr) and the angles between the primitive cell vectors (deg) of Li_xMnPO_4 ($x = 0, 0.5, 1$) computed with DFT (GGA at the PBEsol level) and with the Hubbard + U and + $U+V$ corrections, and compared with available experimental values (the superscripts a and b indicate Refs. [175] and [166], respectively).

		GGA	DFT+ U	DFT+ $U+V$	Expt.
LiMnPO_4	a	19.62	19.94	19.79	19.76 ^a , 19.71 ^b
	b/a	0.58	0.58	0.58	0.58 ^{a,b}
	c/a	0.45	0.45	0.45	0.45 ^{a,b}
$\text{Li}_{0.5}\text{MnPO}_4$	a	18.74	19.39	19.19	n/a
	b/a	0.61	0.61	0.60	
	c/a	0.48	0.47	0.47	
	α	90.02	90.0	89.78	
	β	88.44	86.93	86.03	
	γ	89.95	90.0	93.35	
MnPO_4	a	18.38	18.94	18.75	18.31 ^b
	b/a	0.61	0.62	0.61	0.61 ^b
	c/a	0.50	0.50	0.51	0.49 ^b

TABLE VII. Atomic occupations of d states, formation energy, and average voltages for Li_xMnPO_4 , computed with different methods and compared with available experimental data. As also noted in Table III for LFPO, DFT+ U + V improves the agreement of the computed voltage with the experimental data and is the only approach to predict charge disproportionation with an accurate description of atomic occupations in the mixed-valence ground state for $x = 0.5$.

	Mn^{2+} ($x = 1$)	$\text{Mn}^{2+}/\text{Mn}^{3+}$ ($x = 0.5$)	Mn^{3+} ($x = 0$)	F. E. (meV/f.u.)	Voltage (V)
GGA	5.30	5.19/5.17	5.11	63	2.82
DFT+ U_{ave}	5.19	5.11/5.05	4.96	212	4.31
DFT+ U	5.18	5.11/5.08	4.98	161	5.14
DFT+ U + V	5.23	5.22/4.99	4.99	206	4.15
Expt.				>0	~4.1

LFPO, deserves special attention. In fact, as evident from Table VI, the lower symmetry of the crystal structure can lead to significant distortions of the unit cell. While GGA and DFT+ U stabilize an effectively monoclinic cell (with only the β angle deviating significantly from 90°), the use of intersite interactions V in the corrective functionals leads to an equilibrium triclinic unit cell with all the angles between cell vectors deviating from 90° .

Table VII reports the total occupation of Mn atoms in the three Mn compounds considered and compares the average voltages and the formation energies for the half-lithiated crystal obtained from different Hubbard corrections. At variance with LFPO, the DFT+ U with on-site only corrections is not effective in capturing the disproportionation of the Löwdin charges in the half-lithiated compound and the difference between the occupation of 2+ and 3+ Mn ions in this case is only marginally larger than that predicted by GGA. When using the intersite V , instead, the occupations of 2+ and 3+ ions are obtained in precise consistency with the fully lithiated (2+) and delithiated (3+) cases, showing the effectiveness of this corrective functional in capturing electronic localization in the presence of significant hybridization. Regarding the formation energies, while they result positive in all the approximations considered, their values increase when a Hubbard correction (of any type) is used, probably due to the destabilization of the metallic ground state that is, instead, obtained from GGA calculations for the half-lithiated material. For the average voltage, however, while GGA significantly underestimates experiments, DFT+ U overestimates them. The best agreement with experimental measurements of this quantity is obtained again within DFT+ U + V . As in the case of LiFePO_4 , in order to fully appreciate the effectiveness of the various Hubbard corrections discussed above, a comparative study between the density of states obtained from these approximations is proposed for one of the materials in the LMPO family, namely MnPO_4 . The delithiated member of the Mn olivine system has not been very much studied, probably due to its poor thermal stability (its tendency to decompose and to release oxygen), actually still under investigation (see, e.g., Ref. [178] and references therein). Its computational characterization has been also quite sporadic with studies predicting either half-metallic [82] or semiconducting [179] behavior. The results of this work are shown in Fig. 5 with the same color convention already used in Fig. 2 for LFPO. For the correct interpretation of these results it is useful to keep in mind that Mn ions are nominally in a 3+ oxidation state in this compound with four electrons in their d shells. Because of

their high-spin configuration, the presence of a hole in their d manifold should result in a majority-spin d state moved above (and separated by an energy gap from) the top of the valence band. As clearly shown in Fig. 5 this is only obtained when a finite intersite interaction V is used in the (extended) Hubbard functional [Fig. 5(c)]. The GGA (PBEsol) functional does in fact yield a nonmetallic ground state (the DOS of the system being 0 at the Fermi level). However, the band gap is quite small, probably due to the well known tendency of this functional to overstabilize partially filled bands and delocalized distributions of electrons, and to its inability to completely emptying the highest energy majority-spin and the minority-spin d states. This result is in agreement with Ref. [179]. In contrast with that work, instead, our DFT+ U calculations do not predict a semiconducting ground state and only result in an upward shift of the energy of minority-spin d states that are minimally overlapping with oxygen p states. The highest energy majority-spin d state of Mn, instead, probably because of its mixed d - p character (as suggested by the presence of both contributions in the peak right above the Fermi level), is predicted to be contiguous with the top of the valence band. The use of the intersite interaction V qualitatively changes these results and, thanks to the more flexible expression of the corrective functional, successfully localizes the hole on the antibonding state formed by a majority-spin Mn d and an O p state, pushing the energy of the corresponding peak of the DOS to higher energy and opening a finite energy gap (of about 1.1–1.3 eV) from the top of the valence band. From the comparison of DFT+ U and DFT+ U + V results it is important to note that the intersite interaction mostly affects the top of the valence band, where the gap opens. In other regions of the energy spectrum its effect seems to be minor, even if the overlap between Mn d and O p states is significant. This insensitivity is probably the result of two opposite factors that compensate each other: a smaller on-site Hubbard U and a finite intersite V (see Table V).

The hybridization-driven band-gap opening and hole localization described above for MPO is analogous to that discussed in Ref. [63] focusing on the localization of an electron/hole polaron in LMPO. In that work DFT+ U was found unable to achieve the full localization of the defect charge and is reported to predict a metallic behavior under all conditions. In order to predict a localized extra charge in the material a hybrid functional was used, whose main effect is to push the energy of the unoccupied majority-spin d state of one Mn ion into the band gap of the material. The results described above, although obtained from charge-neutral cal-

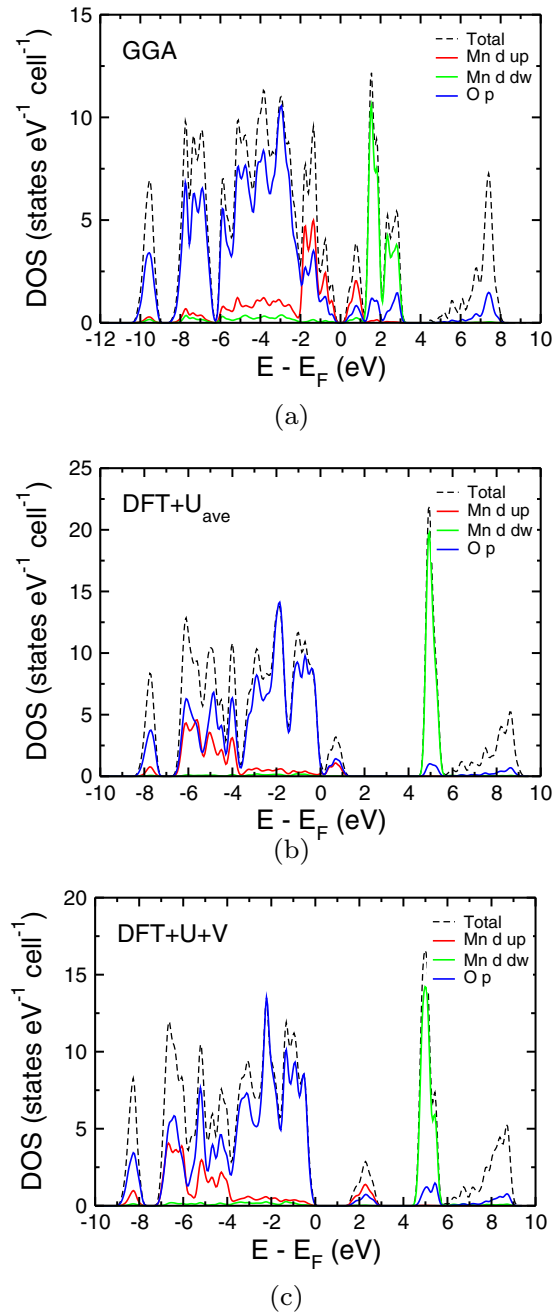


FIG. 5. The density of states of MnPO_4 obtained with different approximations: GGA (PBEsol) (a), $\text{DFT}+U_{\text{ave}}$ (b), and $\text{DFT}+U+V$ (c). In all the graphs the black dashed line represents the total density of state while solid red, green, and blue ones designate manganese d state spin up, manganese d state spin down, and oxygen p states total contributions. All energies are referred to the Fermi level or to the top of the valence band in the presence of a gap.

culations, suggest that $\text{DFT}+U+V$ could achieve a similar result.

As in the case of LFPO, the results presented above are validated by a series of self-consistent calculations including structural optimizations and Hubbard parameters evaluations from the DFPT [109]. The results of these calculations are detailed in the Supplemental Material [108] that develops a comparative analysis. Overall, $\text{DFT}+U+V$ calculations em-

ploying DFPT to compute the Hubbard parameters confirm the results discussed above both quantitatively (the average voltage is 4.21 V) and qualitatively, highlighting their convergence and robustness. A somewhat wider variation is instead noted for $\text{DFT}+U$ calculations that seem more delicate to converge self-consistently.

2. Li ion and magnetic configurations

As anticipated at the beginning of this section, the same magnetic configurations considered for the Fe-based system are also compared for LMPO. The total energies have the same ordering as in LFPO ($E_{\text{AF}_1} < E_{\text{AF}_2} < E_{\text{AF}_3} < E_{\text{FM}}$) with the ground state also in the AF_1 configuration. The energy differences between these different magnetic orders and the AF_1 ground state show a moderate dependence on the approximation being adopted (while the ordering is robust). In particular, the energy differences are (in meV per formula unit): 2.2, 12.3, and 15.5 from $\text{DFT}+U+V$ and 4.7, 35.4, and 43.4 in GGA (PBEsol) calculations. In analogy with LiFePO_4 these energy differences are irrelevant for the evaluation of formation energies and average voltages. Their small value (actually comparable with the precision of our calculation) suggest that all these magnetic configurations can be reached even at moderate temperatures.

Of greater interest is the comparison between the two Li configurations for the $x = 0.5$ compound. Based on the clear improvement brought about by the extended $\text{DFT}+U+V$ scheme compared to other Hubbard flavors, as evident from the results presented in the previous section, calculations were performed only with this functional and with uncorrected GGA for comparison. As in the case of LiFePO_4 , the configuration with Li filling alternate xz planes has lower energy than the one with Li on alternate yz planes and results in about 255 (105) meV per formula unit more stable with $\text{DFT}+U+V$ (GGA). At the same time the formation energy of the xz structure thus amounts to 58 (−42) meV per formula unit with $\text{DFT}+U+V$ (GGA), which is of the same order of magnitude of the analogous structure of the Fe olivine. The rearrangement of the crystal structure is, however, more pronounced than in the case of the Fe olivine, consistently with the fact that the Mn^{3+} ions are Jahn-Teller active and typically induce more pronounced distortions to the octahedral oxygen cages around them. Figure 6 compares the unit cells of $\text{Li}_{0.5}\text{MnPO}_4$ with Li ions on alternate yz [Figs. 6(a) and 6(c)] and xz planes [Figs. 6(b) and 6(d)]. Consistently with the case of LFPO these cells will be referred to as yz and xz cells. As can be seen already from a visual comparison between Figs. 6(a) and 6(b), the xz cell regularizes its shape and almost completely recovers an orthorhombic symmetry. In fact, its equilibrium lattice parameters (bohrs) and angles (deg) are: $a = 19.20$, $b = 11.59$, $c = 9.15$, $\alpha = \beta = 90.0$, and $\gamma = 90.36$. At the same time, when Li atoms fully occupy alternate xz planes, the system undergoes a significant distortion of its internal coordinates. A particularly relevant aspect of this distortion is the fact that Li cations lose their alignment along the [010] crystalline direction and configure themselves in a zigzag pattern (with more complicated arrangements possibly emerging from bigger supercells of larger extension along b). This fact is quite evident from Figs. 6(c) and 6(d) that, in fact,

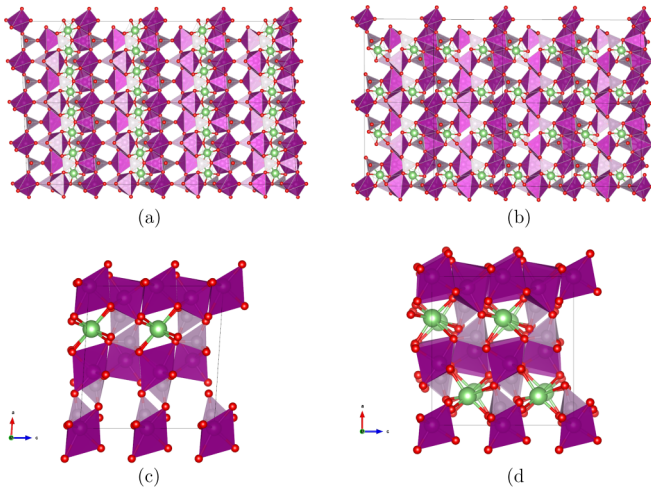


FIG. 6. The two Li configurations of $\text{Li}_{0.5}\text{MnPO}_4$ considered in this work with Li ions occupying alternate yz planes (a) and (c) or xz planes (b) and (d). The figure compares views of a $4 \times 4 \times 2$ supercell of the crystals along the $[001]$ (a) and (b) and along the $[010]$ (c) and (d) directions.

offer a view of the unit cell normal to the xz planes (i.e., along the $[010]$ direction). Based on the consolidated idea that Li motion takes place along the $[010]$ direction in olivine phosphates [142,180], the observation above could provide an important element to explain the low ionic conductivity of the Mn compound (especially in comparison with the Fe olivine). In fact, the diffusion of Li ions during the charge and discharge transients moves the interface between the $x = 1$ and $x = 0$ regions of the cathode. If a $x = 0.5$ phase is stabilized at this interface (e.g., by a reduction of the interfacial stress between the two phases), Li ions have to diffuse through the half-lithiated crystal. While the xz half-lithiated structure would be favored by its lower formation energy and a higher degree of structural compatibility with the $x = 0, 1$ crystals (both orthorhombic), the zigzag ordering of the Li ions and, in general, a more distorted internal structure, could substantially impair the diffusion of these ions along the preferred $[010]$ direction and thus compromise the ionic conductivity of the electrode or the capability of the boundary to move.

The structural rearrangement that is observed between the two Li configurations also reflects a different distribution of valence electrons (a different spatial configuration of 2+ and 3+ Mn cations). However, as in the case of the Fe olivine, the Mn ions that result closer to the Li atoms consistently assume a 2+ state, while the others result in a 3+ state. Their total d states occupations, approximately equal to 5.21 and 4.97 are, again, consistent with those of the yz configuration for Mn ions in corresponding oxidation states and shown in Tables VII and S.VI for DFT+ U + V and DFT+ U + $V_{1 \times 2 \times 2}$ (5.22/4.99 and 5.21/4.98, respectively). The values of the (self-consistent) Hubbard U obtained for the Mn 2+ and 3+ species are, respectively, 4.71 and 6.70 eV, in quite good agreement with the ones computed for the yz structure and presented in Tables V and S.IV. The values of the Hubbard V (0.42–1.35 and 0.28–1.03 eV, respectively) show instead a much looser resemblance with those in the same tables, probably due to difference in the local crystal structure around

Mn ions in corresponding states in the two configurations. In fact we also note that while distances between Mn and their neighbor O ions are quite similar (except for the most distant two oxygens) for the transition-metal ions in 3+ states, for the 2+ ions the oxygen cages are somewhat different. In addition, in the xz configuration Mn ions are always closer to the nearest Li, which seems to suggest a higher binding energy between Li ions and moving electrons, also corroborating the idea that the xz configuration is characterized by a low (ionic and electronic) conductivity.

V. SUMMARY

In this work we have used an extended formulation of DFT+ U , named DFT+ U + V [107], to perform first-principles calculations on two important transition-metal olivine phosphates, Li_xFePO_4 and Li_xMnPO_4 , that are studied as materials for cathodes of Li-ion batteries. The new computational tool employed in these calculations is characterized by a corrective functional based on an extended Hubbard Hamiltonian that contains both on-site (U) and intersite (V) effective interactions. These electronic interaction parameters, computed for all the TM species (crystallographic site, magnetic and oxidation state) present, are calculated from first principles using linear-response theory [78] and, through a recursive self-consistent procedure, are obtained in full consistency with both the electronic and crystal structures. Computing the energetics of the above-mentioned materials at various Li contents and evaluating key quantities to assess their performance as the average voltage, this work develops a thorough comparison between the results obtained from DFT+ U + V , and those of standard DFT functionals, such as PBEsol, or on-site only Hubbard corrections (DFT+ U), using either an effective Hubbard U computed for each Li concentration, or averaged over the entire chemical composition range, as often done in literature. The comparative analysis is completed by contrasting the computed quantities with experimental data, when available.

The results demonstrate that (i) material- and site-specific interaction parameters can be used confidently (provided they are evaluated self-consistently) in energy comparisons without any need of averaging over composition ranges and (ii) the addition of the intersite interaction (V) to the corrective Hubbard functionals improves significantly the accuracy of the approach and extends considerably the range of electronic localization regimes that can be successfully described. For Li_xFePO_4 , the more ionic of the two systems, the improvement that this extension brings is mostly quantitative: it corrects the width of the band gap of the material, refines the equilibrium crystal structure, and, most notably, improves the value of the average voltages, delivering all these quantities in better agreement with available experimental data. For Li_xMnPO_4 , the inclusion of the intersite coupling leads also to a qualitative improvement on the results of simpler approximations. In fact, this material features a more pronounced hybridization between the transition metal ions and their nearest neighbor oxygens and a Hubbard corrective functional with on-site only interactions (i.e., DFT+ U) is not capable to capture electronic localization (e.g., on the Mn^{2+} ions at $x = 0.5$) and overcorrects important quantities such as the average

voltage. The inclusion of the intersite interaction V leads to a more refined description of hybridized states that captures charge disproportionation at intermediate Li content (i.e., a clear distinction of Mn ions in 2+ and 3+ with occupations separately similar to those of lithiated and delithiated materials), refines the equilibrium crystal structure and the agreement with the lattice parameters measured in experiments (albeit not uniformly for all compositions), and improves the prediction of the average voltage vs Li/Li⁺. The use of the extended Hubbard functional also allows us to capture a significant reorganization of the internal structure of the crystal upon changing Li configuration at intermediate compositions (probably a consequence of the Jahn-Teller activity of Mn³⁺ ions) that suggests a stronger binding than in the Fe olivine between Li⁺ and incoming electrons and higher kinetic barriers for Li ions to overcome during their diffusion. To further test the predictivity of the extended DFT+ U + V functional we have also performed calculations on the mixed Fe-Mn olivine phosphate Li_{*x*}Mn_{*y*}Fe_{1-*y*}PO₄ (see Ref. [105] for a useful review on this system). Preliminary calculations (whose results will be published elsewhere) on this system have shown that DFT+ U + V is also able to capture charge disproportionation in the presence of multiple transition-metal species with occupations that are consistent with those shown in this paper for both Fe and Mn in all the oxidation states explored. In addition, it correctly predicts Mn³⁺ ions in the delithiated compound to be the first to reduce upon Li intercalation.

From a methodological point of view the accuracy and predictivity that the extended DFT+ U + V functional achieves with a consistent calculation of the Hubbard parameters is quite remarkable, especially in comparison with the very abundant literature where the simpler on-site only DFT+ U is used with a semiempirical tuning of the interaction parameters on the properties of interest. Notwithstanding the fact that the semiempirical evaluation of interaction parameters is impossible without reference (e.g., experimental results to fit) and is far less viable with more advanced functionals (e.g., including several kinds of interactions) or when multiple Hubbard species (or oxidation states) are present, it should be also kept in mind that within DFT+ U it is often impossible to iden-

tify a single set of Hubbard parameters able to improve the prediction of all the properties of a system [88–90]. In other words if a value of U is needed to reproduce the equilibrium crystal structure, the one(s) necessary to improve for example the prediction of the magnetic moment, of the band gap, or of the energetics of certain processes (as Li intercalation) is (are) likely to be quite different. We believe that the results of this work show quite clearly that DFT+ U + V with Hubbard parameters evaluated self-consistently from LRT represents a significant step forward in this respect as it not only allows us to confidently approach the study of a much broader spectrum of different materials, but is also capable of improving the prediction of several properties at the same time. The recent automation of the LRT evaluation of the Hubbard parameters through DFPT [109], reducing significantly its computational cost and improving its robustness, user friendliness, and accuracy, is thus making self-consistent DFT+ U + V emerge as a predictive, versatile, and efficient tool for the accurate modeling of a broad variety of materials (especially when their functionality is related to electronic localization) and for the discovery and optimization of new ones through large-scale high-throughput *ab initio* calculations.

ACKNOWLEDGMENTS

Partial financial support for this work was provided by the Max Planck - EPFL center for Molecular Nanoscience and Technology, by the Swiss National Science Foundation through Grant No. 200021-179138 and its National Centre of Competence in Research (NCCR) MARVEL, and from the EU-H2020 research and innovation programme under Grant Agreement No. 654360 within the framework of the NFFA-Europe Transnational Access Activity. We are grateful to Prof. J. Maier and Prof. B. Lotsch for suggesting this as an important case study. The calculations presented in this paper were performed using computational resources made available by the Swiss National Supercomputing Centre (CSCS), through Grants s580 and s836. Figures containing crystal structures (Figs. 1, 3, 4, and 6) were all realized using the VESTA crystal visualization software [181].

-
- [1] J. Liu, C. Xu, Z. Chen, S. Ni, and Z. X. Shen, Progress in aqueous rechargeable batteries, *Green Energy Environ.* **3**, 20 (2018).
 - [2] K. Kei, D. Mouad, H. Tomooki, K. Shinichi, and K. Shinichi, Towards K-ion and Na-ion batteries as “beyond Li-ion”, *Chem. Record* **18**, 459 (2018).
 - [3] H. Kim, J. C. Kim, M. Bianchini, D.-H. Seo, J. Rodriguez-Garcia, and G. Ceder, Recent progress and perspective in electrode materials for K-ion batteries, *Adv. Energy Mater.* **8**, 1702384 (2018).
 - [4] R. K. Guduru and J. C. Icaza, A brief review on multivalent intercalation batteries with aqueous electrolytes, *Nanomaterials* **6**, 41 (2016).
 - [5] J. Christensen *et al.*, A critical review of Li/air batteries, *J. Electrochem. Soc.* **159**, R1 (2012).
 - [6] K.-N. Jung, J. Kim, Y. Yamauchi, M.-S. Park, J.-W. Lee, and J. H. Kim, Rechargeable lithium-air batteries: A perspective on the development of oxygen electrodes, *J. Mater. Chem. A* **4**, 14050 (2016).
 - [7] Y. Yuan, K. Amine, J. Lu, and R. Shahbazian-Yassar, Understanding materials challenges for rechargeable ion batteries with in situ transmission electron microscopy, *Nat. Commun.* **8**, 15806 (2017).
 - [8] D. Denga, Li-ion batteries: Basics, progress, and challenges, *Energy Sci. Eng.* **3**, 385 (2015).
 - [9] V. Etacheri, R. Marom, R. Elazari, G. Salitra, and D. Aurbach, Challenges in the development of advanced Li-ion batteries: A review, *Energy Environ. Sci.* **4**, 3243 (2011).
 - [10] N. Recham, J.-N. Chotard, L. Dupont, C. Delacourt, W. Walker, M. Armand, and J.-M. Tarascon, A 3.6 V lithium-based fluorosulphate insertion positive electrode for lithium-ion batteries, *Nat. Mater.* **9**, 68 (2010).
 - [11] M. Armand and J.-M. Tarascon, Building better batteries, *Nature (London)* **451**, 652 (2008).

- [12] C. M. Hayner, X. Zhao, and H. H. Kung, Materials for rechargeable lithium-ion batteries, *Annu. Rev. Chem. Biomol. Eng.* **3**, 445 (2012).
- [13] N. Nitta, F. Wu, J. T. Lee, and G. Yushin, Li-ion battery materials: Present and future, *Mater. Today* **18**, 252 (2015).
- [14] Y. Mekkonen, A. Sundararajan, and A. I. Sarwat, *A Review of Cathode and Anode Materials for Lithium-Ion Batteries* (IEEE, Piscataway, NJ, 2016), pp. 1–6.
- [15] F. Zheng, M. Kotobuki, S. Song, M. O. Lai, and L. Lu, Review on solid electrolytes for all-solid-state lithium-ion batteries, *J. Power Sources* **389**, 198 (2018).
- [16] Y. Meesala, A. Jena, H. Chang, and R.-S. Liu, Recent advancements in Li-ion conductors for all-solid-state Li-ion batteries, *ACS Energy Lett.* **2**, 2734 (2017).
- [17] J. C. Bachman, S. Muy, A. Grimaud, H.-H. Chang, N. Pour, S. F. Lux, O. Paschos, F. Maglia, S. Lupart, P. Lamp, L. Giordano, and Y. Shao-Horn, Inorganic solid-state electrolytes for lithium batteries: Mechanisms and properties governing ion conduction, *Chem. Rev.* **116**, 140 (2016).
- [18] C. Ma and M. Chi, Novel solid electrolytes for Li-ion batteries: A perspective from electron microscopy studies, *Frontiers Energy Res.* **4**, 23 (2016).
- [19] B. V. Lotsch and J. Maier, Relevance of solid electrolytes for lithium-based batteries: A realistic view, *J. Electroceram.* **38**, 128 (2017).
- [20] J. B. Goodenough and P. Singh, Review—Solid Electrolytes in Rechargeable Electrochemical Cells, *J. Electrochem. Soc.* **162**, A2387 (2015).
- [21] A. Kuhn, O. Gerbig, C. Zhu, F. Falkenberg, J. Maier, and B. V. Lotsch, A new ultrafast superionic Li-conductor: Ion dynamics in $\text{Li}_{11}\text{Si}_2\text{PS}_{12}$ and comparison with other tetragonal LGPS-type electrolytes, *Phys. Chem. Chem. Phys.* **16**, 14669 (2014).
- [22] M. H. Braga, N. S. Grundish, A. J. Murchison, and J. B. Goodenough, Alternative strategy for a safe rechargeable battery, *Energy Environ. Sci.* **10**, 331 (2017).
- [23] C. Frayret, A. Villesuzanne, N. Spaldin, E. Bousquet, J.-N. Chotard, N. Recham, and J.-M. Tarascon, LiMSO_4F (M = Fe, Co, and Ni): Promising new positive electrode materials through the DFT microscope, *Phys. Chem. Chem. Phys.* **12**, 15512 (2010).
- [24] T. Richard Jow, J. L. Allen, O. A. Borodin, S. A. Delp, and J. L. Allen, Challenges in developing high energy density Li-ion batteries with high voltage cathodes, in *TMS 2014: 143rd Annual Meeting & Exhibition, Cham* (Springer, Berlin, 2016), pp. 853–857.
- [25] F. Schipper, P. Nayak, E. Erickson, S. Amalraj, O. Srur-Lavi, T. Penki, M. Talianker, J. Grinblat, H. Sclar, O. Breuer *et al.*, Study of cathode materials for lithium-ion batteries: Recent progress and new challenges, *Inorganics* **5**, 32 (2017).
- [26] J. Lu and K. S. Lee, Spinel cathodes for advanced lithium ion batteries: A review of challenges and recent progress, *Mater. Technol.* **31**, 628 (2016).
- [27] J. Lee, J. K. Papp, J. Clément, S. Sallis, D.-H. Kwon, T. Shi, W. Yang, B. D. McCloskey, and G. Ceder, Mitigating oxygen loss to improve the cycling performance of high capacity cation-disordered cathode materials, *Nat. Commun.* **8**, 981 (2017).
- [28] N. Twu, X. Li, A. Urban, M. Balasubramanian, J. Lee, L. Liu, and G. Ceder, Designing new lithium-excess cathode materials from percolation theory: Nanohighways in $\text{Li}_x\text{Ni}_{2-4x/3}\text{Sb}_{x/3}\text{O}_2$, *Nano Lett.* **15**, 596 (2015).
- [29] J. Lee, A. Urban, X. Li, D. Su, G. Hautier, and G. Ceder, Unlocking the potential of cation-disordered oxides for rechargeable lithium batteries, *Science* **343**, 519 (2014).
- [30] A. Kraytsberg and Y. Ein-Eli, Higher, stronger, better... A review of 5 Volt cathode materials for advanced lithium-ion batteries, *Adv. Energy Mater.* **2**, 922 (2012).
- [31] C. Li, X. Mu, P. A. van Aken, and J. Maier, A high-capacity cathode for lithium batteries consisting of porous microspheres of highly amorphized iron fluoride densified from its open parent phase, *Adv. Energy Mater.* **3**, 113 (2013).
- [32] F. Wang, S.-W. Kim, D.-H. Seo, K. Kang, L. Wang, D. Su, J. J. Vajo, J. Wang, and J. Graetz, Ternary metal fluorides as high-energy cathodes with low cycling hysteresis, *Nat. Commun.* **6**, 6668 (2015).
- [33] P. Rozier and J. M. Tarascon, Review—Li-rich layered oxide cathodes for next-generation Li-ion batteries: Chances and challenges, *J. Electrochem. Soc.* **162**, A2490 (2015).
- [34] L. Wang, Y. Lu, J. Liu, M. Xu, J. Cheng, D. Zhang, and J. B. Goodenough, A superior low-cost cathode for a Na-ion battery, *Angew. Chem. Intl. Ed.* **52**, 1964 (2013).
- [35] G. Hautier, Prediction of new battery materials based on *ab initio* computations, in *Proceedings of the 2nd International Freiberg Conference on Electrochemical Storage Materials: Supply, Processing, Recycling and Modelling*, edited by T. Leisegang, AIP Conf. Proc. No. 1765 (AIP, New York, 2016), p. 020009.
- [36] G. Ceder, Y.-M. Chiang, D. R. Sadoway, M. K. Aydinol, Y.-I. Jang, and B. Huang, Identification of cathode materials for lithium batteries guided by first-principles calculations, *Nature* **392**, 694 (1998).
- [37] G. Ceder, M. K. Aydinol, and A. F. Kohan, Application of first-principles calculations to the design of rechargeable Li-batteries, *Comput. Mater. Sci.* **8**, 161 (1997).
- [38] R. Pigliapochi, A. J. Pell, I. D. Seymour, C. P. Grey, D. Ceresoli, and M. Kaupp, DFT investigation of the effect of spin-orbit coupling on the NMR shifts in paramagnetic solids, *Phys. Rev. B* **95**, 054412 (2017).
- [39] X. Liu *et al.*, Phase transformation and lithiation effect on electronic structure of Li_xFePO_4 : An in-depth study by soft x-ray and simulations, *J. Am. Chem. Soc.* **134**, 13708 (2012).
- [40] T. Maxisch, F. Zhou, and G. Ceder, *Ab initio* study of the migration of small polarons in olivine Li_xFePO_4 and their association with lithium ions and vacancies, *Phys. Rev. B* **73**, 104301 (2006).
- [41] R. Malik, F. Zhou, and G. Ceder, Kinetics of non-equilibrium lithium incorporation in LiFePO_4 , *Nat. Mater.* **10**, 587 (2011).
- [42] M. F. Sgroi, R. Lazzarone, D. Beljonne, and D. Pullini, Doping LiMnPO_4 with cobalt and nickel: A first principle study, *Batteries* **3**, 11 (2017).
- [43] A. Van der Ven, M. K. Aydinol, G. Ceder, G. Kresse, and J. Hafner, First-principles investigation of phase stability in Li_xCoO_2 , *Phys. Rev. B* **58**, 2975 (1998).
- [44] C. Wolverton and A. Zunger, First-Principles Prediction of Vacancy Order-Disorder and Intercalation Battery Voltages in Li_xCoO_2 , *Phys. Rev. Lett.* **81**, 606 (1998).
- [45] A. Van der Ven, K. Garikipati, S. Kim, and M. Wagemaker, The role of coherency strains on phase stability in Li_xFePO_4 : Needle crystallites minimize coherency strain and overpotential, *J. Electrochem. Soc.* **156**, A949 (2009).

- [46] G. K. P. Dathar, D. Sheppard, K. J. Stevenson, and G. Henkelman, Calculations of Li-ion diffusion in olivine phosphates, *Chem. Mater.* **23**, 4032 (2011).
- [47] Y. M. Yiu, S. Yang, D. Wang, X. Sun, and T. K. Sham, Ab-initio calculation of the XANES of lithium phosphates and Li_xFePO_4 , *J. Phys.: Conf. Series* **430**, 012014 (2013).
- [48] J. Yang and J. S. Tse, Li ion diffusion mechanisms in LiFePO_4 : An ab Initio molecular dynamics study, *J. Phys. Chem. A* **115**, 13045 (2011).
- [49] Y. Zhang, A. Castets, D. Carlier, M. Ménétrier, and F. Boucher, Simulation of NMR Fermi contact shifts for lithium battery materials: The need for an efficient hybrid functional approach, *J. Phys. Chem.* **116**, 17393 (2012).
- [50] Y. Sun, X. Lu, R. Xiao, H. Li, and X. Huang, Kinetically controlled lithium-staging in delithiated LiFePO_4 driven by the Fe center mediated interlayer Li-Li interactions, *Chem. Mater.* **24**, 4693 (2012).
- [51] S. Xu, R. Jacobs, C. Wolverton, T. Kuech, and D. Morgan, Nanoscale voltage enhancement at cathode interfaces in Li-ion batteries, *Chem. Mater.* **29**, 1218 (2017).
- [52] M. Catti, *Ab initio* study of Li1 diffusion paths in the monoclinic $\text{Li}_{0.5}\text{CoO}_2$ intercalate, *Phys. Rev. B* **61**, 1795 (2000).
- [53] D. S. Middlemiss, A. J. Ilott, R. J. Clément, F. C. Strobridge, and C. P. Grey, Density functional theory-based bond pathway decompositions of hyperfine shifts: Equipping solid-state NMR to characterize atomic environments in paramagnetic materials, *Chem. Mater.* **25**, 1723 (2013).
- [54] B. C. Han, A. Van der Ven, D. Morgan, and G. Ceder, Electrochemical modeling of intercalation processes with phase field models, *Electrochim. Acta* **49**, 4691 (2004).
- [55] P. Hohenberg and W. Kohn, Inhomogeneous electron gas, *Phys. Rev.* **136**, B864 (1964).
- [56] W. Kohn and L. J. Sham, Self-consistent equations including exchange and correlation effects, *Phys. Rev.* **140**, A1133 (1965).
- [57] J. Sun, A. Ruzsinszky, and J. P. Perdew, Strongly Constrained and Appropriately Normed Semilocal Density Functional, *Phys. Rev. Lett.* **115**, 036402 (2015).
- [58] A. Chakraborty, M. Dixit, D. Aurbach, and D. T. Major, Predicting accurate cathode properties of layered oxide materials using the SCAN meta-GGA density functional, *npj Comput. Mater.* **4**, 60 (2018).
- [59] D. A. Kitchaev, H. Peng, Y. Liu, J. P. Perdew, and G. Ceder, Energetics of MnO_2 polymorphs in density functional theory, *Phys. Rev. B* **93**, 045132 (2016).
- [60] Y. Zhang, D. A. Kitchaev, J. Yang, T. Chen, S. T. Dacek, R. A. Sarmiento-Pérez, M. A. L. Marques, H. Peng, G. Ceder, J. P. Perdew, and J. Sun, Efficient first-principles prediction of solid stability: Towards chemical accuracy, *npj Comput. Mater.* **4**, 9 (2018).
- [61] E. B. Isaacs and C. Wolverton, Performance of the strongly constrained and appropriately normed density functional for solid-state materials, *Phys. Rev. Mater.* **2**, 063801 (2018).
- [62] A. Urban, D.-H. Seo, and G. Ceder, Computational understanding of Li-ion batteries, *npj Comput. Mater.* **2**, 16002 (2016).
- [63] S. Ping Ong, V. L. Chevrier, and G. Ceder, Comparison of small polaron migration and phase separation in olivine LiMnPO_4 and LiFePO_4 using hybrid density functional theory, *Phys. Rev. B* **83**, 075112 (2011).
- [64] V. I. Anisimov, M. A. Korotin, and E. Z. Kurmaev, Band-structure description of Mott insulators (NiO , MnO , FeO , CoO), *J. Phys.: Condens. Matter* **2**, 3973 (1990).
- [65] V. I. Anisimov and O. Gunnarsson, Density-functional calculation of effective Coulomb interactions in metals, *Phys. Rev. B* **43**, 7570 (1991).
- [66] A. I. Liechtenstein, V. I. Anisimov, and J. Zaanen, Density-functional theory and strong interactions: Orbital ordering in Mott-Hubbard insulators, *Phys. Rev. B* **52**, R5467 (1995).
- [67] V. I. Anisimov, F. Aryasetiawan, and A. I. Liechtenstein, First-principles calculations of the electronic structure and spectra of strongly correlated systems: the LDA + U method, *J. Phys.: Condens. Matter* **9**, 767 (1997).
- [68] S. L. Dudarev, G. A. Botton, S. Y. Savrasov, C. J. Humphreys, and A. P. Sutton, Electron-energy-loss spectra and the structural stability of nickel oxide: An LSDA+U study, *Phys. Rev. B* **57**, 1505 (1998).
- [69] V. I. Anisimov, J. Zaanen, and O. K. Andersen, Band theory and Mott insulators: Hubbard U instead of Stoner I, *Phys. Rev. B* **44**, 943 (1991).
- [70] I. V. Solov'ev, P. H. Dederichs, and V. I. Anisimov, Corrected atomic limit in the local-density approximation and the electronic structure of *d* impurities in Rb, *Phys. Rev. B* **50**, 16861 (1994).
- [71] I. I. Mazin and V. I. Anisimov, Insulating gap in FeO: Correlations and covalency, *Phys. Rev. B* **55**, 12822 (1997).
- [72] W. E. Pickett, S. C. Erwin, and E. C. Ethridge, Reformulation of the LDA+U method for a local-orbital basis, *Phys. Rev. B* **58**, 1201 (1998).
- [73] H. J. Kulik, M. Cococcioni, D. A. Scherlis, and N. Marzari, Density Functional Theory in Transition-Metal Chemistry: A Self-Consistent Hubbard *U* Approach, *Phys. Rev. Lett.* **97**, 103001 (2006).
- [74] H. J. Kulik and N. Marzari, A self-consistent Hubbard *U* density-functional theory approach to the addition-elimination reactions of hydrocarbons on bare FeO^+ , *J. Chem. Phys.* **129**, 134314 (2008).
- [75] F. Zhou, C. A. Marianetti, M. Cococcioni, D. Morgan, and G. Ceder, Phase separation in Li_xFePO_4 induced by correlation effects, *Phys. Rev. B* **69**, 201101(R) (2004).
- [76] F. Zhou, M. Cococcioni, C. A. Marianetti, D. Morgan, and G. Ceder, First-principles prediction of redox potentials in transition-metal compounds with LDA+U, *Phys. Rev. B* **70**, 235121 (2004).
- [77] F. Zhou, M. Cococcioni, K. Kang, and G. Ceder, The Li intercalation potential of LiMPO_4 and LiMSiO_4 olivines with $M = \text{Fe, Mn, Co, Ni}$, *Electrochem. Comm.* **6**, 1144 (2004).
- [78] M. Cococcioni and S. de Gironcoli, Linear response approach to the calculation of the effective interaction parameters in the LDA+U method, *Phys. Rev. B* **71**, 035105 (2005).
- [79] E. B. Isaacs and C. A. Marianetti, Compositional phase stability of strongly correlated electron materials within DFT+U, *Phys. Rev. B* **95**, 045141 (2017).
- [80] S. Loftager, J. M. García-Lastra, and T. Vegge, A Density Functional Theory Study of the Ionic and Electronic Transport Mechanism in LiFeBO_3 Battery Electrodes, *J. Phys. Chem. C* **120**, 18355 (2016).
- [81] M. Shishkin and H. Sato, Self-consistent parametrization of DFT+*U* framework using linear response approach:

- Application to evaluation of redox potentials of battery cathodes, *Phys. Rev. B* **93**, 085135 (2016).
- [82] T.-F. Yi, Z.-K. Fang, Y. Xie, Y.-R. Zhu, and C. Dai, Band structure analysis on olivine LiMPO_4 and delithiated MPO_4 ($M = \text{Fe}, \text{Mn}$) cathode materials, *J. Alloys Comp.* **617**, 716 (2014).
- [83] A. Bhowmik, T. Sarkar, A. K. Varanasi, U. V. Waghmare, and M. Dixit Bharadwaj, Origins of electrochemical performance of olivine phosphate as cathodes in Li-ion batteries: Charge transfer, spin-state, and structural distortion, *J. Renewable Sustainable Energy* **5**, 053130 (2013).
- [84] S. Leoni, M. Baldoni, L. Craco, J. O. Joswig, and G. Seifert, Materials for lithium ion batteries: Challenges for numerical simulations, *Z. Phys. Chem.* **226**, 95 (2012).
- [85] J. Yu, K. M. Rosso, and J. Liu, Charge localization and transport in lithiated olivine phosphate materials, *J. Phys. Chem. C* **115**, 25001 (2011).
- [86] F. Zhou, T. Maxisch, and G. Ceder, Configurational Electronic Entropy and the Phase Diagram of Mixed-Valence Oxides: The Case of Li_xFePO_4 , *Phys. Rev. Lett.* **97**, 155704 (2006).
- [87] O. Le Bacq, A. Pasturel, and O. Bengone, Impact on electronic correlations on the structural stability, magnetism, and voltage of LiCoPO_4 batteries, *Phys. Rev. B* **69**, 245107 (2004).
- [88] J. A. Santana, J. Kim, P. R. C. Kent, and F. A. Reboredo, Successes and failures of Hubbard-corrected density functional theory: The case of Mg doped LiCoO_2 , *J. Chem. Phys.* **141**, 164706 (2014).
- [89] A. Muratahan and C. Wolverton, Local environment dependent GGA+U method for accurate thermochemistry of transition metal compounds, *Phys. Rev. B* **90**, 115105 (2014).
- [90] M. Shishkin and H. Sato, Challenges in computational evaluation of redox and magnetic properties of Fe-based sulfate cathode materials of Li- and Na-ion batteries, *J. Phys.: Condens. Matter* **29**, 215701 (2017).
- [91] J. Wu *et al.*, *In situ* Raman spectroscopy of LiFePO_4 : Size and morphology dependence during charge and self-discharge, *Nanotechnology* **24**, 424009 (2013).
- [92] M. Nakayama, S. Yamada, R. Jalem, and T. Kasuga, Density functional studies of olivine-type LiFePO_4 and NaFePO_4 as positive electrode materials for rechargeable lithium and sodium ion batteries, *Solid State Ionics* **286**, 40 (2016).
- [93] M. D. Johannes, K. Hoang, J. L. Allen, and K. Gaskell, Hole polaron formation and migration in olivine phosphate materials, *Phys. Rev. B* **85**, 115106 (2012).
- [94] D.-H. Seo, A. Urban, and G. Ceder, Calibrating transition-metal energy levels and oxygen bands in first-principles calculations: Accurate prediction of redox potentials and charge transfer in lithium transition-metal oxides, *Phys. Rev. B* **92**, 115118 (2015).
- [95] V. L. Chevrier, P. S. Ong, R. Armiento, M. K. Y. Chan, and G. Ceder, Hybrid density functional calculations of redox potentials and formation energies of transition metal compounds, *Phys. Rev. B* **82**, 075122 (2010).
- [96] A. K. Padhi, K. S. Nanjundaswamy, and J. B. Goodenough, Phospho-olivines as positive-electrode materials for rechargeable lithium batteries, *J. Electrochem. Soc.* **144**, 1189 (1997).
- [97] H. Liu, F. C. Strobridge, O. J. Borkiewicz, K. M. Wiaderek, K. W. Chapman, P. J. Chupas, and C. P. Grey, Capturing metastable structures during high-rate cycling of LiFePO_4 nanoparticle electrodes, *Science* **344**, 1252817 (2014).
- [98] J. Niu, A. Kushima, X. Qiang, Liang Qi, K. Xiang, Y.-M. Chiang, and J. Li, In situ observation of random solid solution zone in LiFePO_4 electrode, *Nano Lett.* **14**, 4005 (2014).
- [99] C. Zhu, L. Gu, L. Suo, J. Popovic, H. Li, Y. Ikuhara, and J. Maier, Size-dependent staging and phase transition in $\text{LiFePO}_4/\text{FePO}_4$, *Adv. Funct. Mater.* **24**, 312 (2014).
- [100] M. Z. Bazant, Theory of chemical kinetics and charge transfer based on nonequilibrium thermodynamics, *Acc. Chem. Res.* **46**, 1144 (2013).
- [101] Y. Orikasa, T. Maeda, Y. Koyama, H. Murayama, K. Fukuda, H. Tanida, H. Arai, E. Matsubara, Z. Uchimoto, and Y. Ogumi, Direct observation of a metastable crystal phase of Li_xFePO_4 under electrochemical phase transition, *J. Am. Chem. Soc.* **135**, 5497 (2013).
- [102] R. Malik, A. Abdellahi, and G. Ceder, A critical review of the Li insertion mechanisms in LiFePO_4 electrodes, *J. Electrochem. Soc.* **160**, A3179 (2013).
- [103] G. Oyama, Y. Yamada, R.-I. Natsui, S.-I. Nishimura, and A. Yamada, Kinetics of nucleation and growth in two-phase electrochemical reaction of Li_xFePO_4 , *J. Phys. Chem. C* **116**, 7306 (2012).
- [104] D. Burch, G. Singh, G. Ceder, and M. Z. Bazant, Phase-transformation wave dynamics in LiFePO_4 , *Solid State Phenom.* **139**, 95 (2008).
- [105] Y. Deng, C. Yang, K. Zou, X. Qin, Z. Zhao, and G. Chen, Recent advances of Mn-rich $\text{LiFe}_{1-y}\text{MnyPO}_4$ ($0.5 \leq y < 1.0$) cathode materials for high energy density lithium ion batteries, *Adv. Energy Mater.* **7**, 1601958 (2017).
- [106] G. Ceder and A. Van der Ven, Phase diagram of lithium transition metal oxides: Investigations from first principles, *Electrochim. Acta* **45**, 131 (1999).
- [107] V. Leiria Campo Jr. and M. Cococcioni, Extended DFT+U+V method with on-site and inter-site electronic interactions, *J. Phys.: Condens. Matter* **22**, 055602 (2010).
- [108] See Supplemental Material at <http://link.aps.org/supplemental/10.1103/PhysRevMaterials.3.033801> for details.
- [109] I. Timrov, N. Marzari, and M. Cococcioni, Hubbard interactions from density-functional perturbation theory, *Phys. Rev. B* **98**, 085127 (2018).
- [110] J. Hubbard, Electron correlations in narrow energy bands, *Proc. R. Soc. London Sect. A* **276**, 238 (1963).
- [111] J. Hubbard, Electron correlations in narrow energy bands. II. The degenerate band case, *Proc. R. Soc. London Sect. A* **277**, 237 (1964).
- [112] J. Hubbard, Electron correlations in narrow energy bands. III. An improved solution, *Proc. R. Soc. London Sect. A* **281**, 401 (1964).
- [113] J. Hubbard, Electron correlations in narrow energy bands. IV. The atomic representation, *Proc. R. Soc. London Sect. A* **285**, 542 (1965).
- [114] J. Hubbard, Electron correlations in narrow energy bands. V. A perturbation expansion about the atomic limit, *Proc. R. Soc. London Sect. A* **296**, 82 (1967).
- [115] J. Hubbard, Electron correlations in narrow energy bands. VI. The connexion with many-body perturbation theory, *Proc. R. Soc. London Sect. A* **296**, 100 (1967).
- [116] B. Himmetoglu, A. Floris, S. de Gironcoli, and M. Cococcioni, Hubbard-corrected DFT energy functionals: The LDA+U

- description of correlated systems, *Int. J. Quant. Chem.* **114**, 14 (2014).
- [117] H. J. Kulik and N. Marzari, Transition-metal dioxides: A case for the intersite term in Hubbard-model functionals, *J. Chem. Phys.* **134**, 094103 (2011).
- [118] H. Hsu, P. Blaha, M. Cococcioni, and R. M. Wentzcovitch, Spin-State Crossover and Hyperfine Interactions of Ferric Iron in (Mg, Fe)SiO₃ Perovskite, *Phys. Rev. Lett.* **106**, 118501 (2011).
- [119] Y. G. Yu, H. Hsu, M. Cococcioni, and R. M. Wentzcovitch, Spin states and hyperfine interactions of iron incorporated in MgSiO₃ post-perovskite, *Earth Planet. Sci. Lett.* **331**, 1 (2012).
- [120] G. Shukla, Z. Wu, H. Hsu, A. Floris, M. Cococcioni, and R. M. Wentzcovitch, Thermoelasticity of Fe²⁺-bearing bridgmanite, *Geophys. Res. Lett.* **42**, 1741 (2015).
- [121] G. Shukla, M. Cococcioni, and R. M. Wentzcovitch, Al-bearing bridgmanite: Effects of iron spin crossover, *Geophys. Res. Lett.* **43**, 5661 (2016).
- [122] G. W. Mann, K. Lee, M. Cococcioni, B. Smit, and J. B. Neaton, First-principles Hubbard U approach for small molecule binding in metal-organic frameworks, *J. Chem. Phys.* **144**, 174104 (2016).
- [123] G. Moynihan, G. Teobaldi, and D. D. O'Regan, A self-consistent ground-state formulation of the first-principles Hubbard U parameter validated on one-electron self-interaction error, [arXiv:1704.08076](https://arxiv.org/abs/1704.08076).
- [124] E. B. Linscott, D. J. Cole, M. C. Payne, and D. D. O'Regan, Role of spin in the calculation of Hubbard U and Hund's J parameters from first principles, *Phys. Rev. B* **98**, 235157 (2018).
- [125] G. Ceder, A. Van der Ven, C. Marianetti, and D. Morgan, First-principles alloy theory in oxides, *Model. Simul. Mater. Sci. Eng.* **8**, 311 (2000).
- [126] A. A. Mbaye, L. G. Ferreira, and Alex Zunger, First-Principles Calculation of Semiconductor-Alloy Phase Diagrams, *Phys. Rev. Lett.* **58**, 49 (1987).
- [127] N. Marzari, S. de Gironcoli, and S. Baroni, Structure and Phase Stability of Ga_xIn_{1-x}P Solid Solutions from Computational Alchemy, *Phys. Rev. Lett.* **72**, 4001 (1994).
- [128] M. Asta, V. Ozolins, and C. Woodward, A first-principles approach to modeling alloy phase equilibria, *JOM* **53**, 16 (2001).
- [129] P. Giannozzi, S. Baroni, N. Bonini, M. Calandra, R. Car, C. Cavazzoni, D. Ceresoli, G. L. Chiarotti, M. Cococcioni, I. Dabo, A. Dal Corso, S. De Gironcoli, S. Fabris, G. Fratesi, R. Gebauer, U. Gerstmann, C. Gougoussis, A. Kokalj, M. Lazzeri, L. Martin-Samos, N. Marzari, F. Mauri, R. Mazzarello, S. Paolini, A. Pasquarello, L. Paulatto, C. Sbraccia, S. Scandolo, G. Sclauzero, A. P. Seitsonen, A. Smogunov, P. Umari, and R. M. Wentzcovitch, Quantum ESPRESSO: A modular and open-source software project for quantum simulations of materials, *J. Phys.: Condens. Matter* **21**, 395502 (2009).
- [130] P. Giannozzi, O. Andreussi, T. Brumme, O. Bunau, M. Buongiorno Nardelli, M. Calandra, R. Car, C. Cavazzoni, D. Ceresoli, M. Cococcioni, N. Colonna, I. Carnimeo, A. Dal Corso, S. de Gironcoli, P. Delugas, R. A. DiStasio Jr., A. Ferretti, A. Floris, G. Fratesi, G. Fugallo, R. Gebauer, U. Gerstmann, F. Giustino, T. Gorni, J. Jia, M. Kawamura, H.-Y. Ko, A. Kokalj, E. Küçükbenli, M. Lazzeri, M. Marsili, N. Marzari, F. Mauri, N. L. Nguyen, H.-V. Nguyen, A. Otero-de-la Rosa, L. Paulatto, S. Poncé, D. Rocca, R. Sabatini, B. Santra, M. Schlipf, A. P. Seitsonen, A. Smogunov, I. Timrov, T. Thonhauser, P. Umari, N. Vast, and S. Baroni, Advanced capabilities for materials modelling with Quantum ESPRESSO, *J. Phys.: Condens. Matter* **29**, 465901 (2017).
- [131] J. P. Perdew, A. Ruzsinszky, G. I. Csonka, O. A. Vydrov, G. E. Scuseria, L. A. Constantin, X. Zhou, and K. Burke, Restoring the Density-Gradient Expansion for Exchange in Solids and Surfaces, *Phys. Rev. Lett.* **100**, 136406 (2008).
- [132] D. Vanderbilt, Soft self-consistent pseudopotentials in a generalized eigenvalue formalism, *Phys. Rev. B* **41**, 7892(R) (1990).
- [133] A. Dal Corso, Pseudopotentials periodic table: From H to Pu, *Comput. Mater. Sci.* **95**, 337 (2014).
- [134] The following pseudopotentials were used: Fe.pbesol-spn-rrkjus-psl.0.2.1.UPF, O.pbesol-n-rrkjus-psl.0.1.UPF, P.pbesol-n-rrkjus-psl.0.1.UPF, Li.pbesol-s-rrkjus-psl.0.2.1.UPF.
- [135] P. Blöchl, Projector augmented-wave method, *Phys. Rev. B* **50**, 17953 (1994).
- [136] E. Kucukbenli, M. Monni, B. I. Adetunji, X. Ge, G. A. Adebayo, N. Marzari, S. de Gironcoli, and A. Dal Corso, Projector augmented-wave and all-electron calculations across the periodic table: A comparison of structural and energetic properties, [arXiv:1404.3015](https://arxiv.org/abs/1404.3015).
- [137] The following pseudopotentials were used: Mn.pbesol-spn-kjpaw-psl.0.3.1.UPF, P.pbesol-n-kjpaw-psl.0.1.UPF, O.pbesol-n-kjpaw-psl.0.1.UPF, Li.pbesol-s-kjpaw-psl.0.2.1.UPF.
- [138] G. Prandini, A. Marrazzo, I. E. Castelli, N. Mounet, and N. Marzari, Precision and efficiency in solid-state pseudopotential calculations, *npj Comput. Mater.* **4**, 72 (2018).
- [139] H. J. Monkhorst and J. D. Pack, Special points for Brillouin-zone integrations, *Phys. Rev. B* **13**, 5188 (1976).
- [140] M. Methfessel and A. T. Paxton, High-precision sampling for Brillouin-zone integration in metals, *Phys. Rev. B* **40**, 3616 (1989).
- [141] L. Craco and S. Leoni, Electrostatics and quantum capacity of Li_xFePO₄ battery material, *Appl. Phys. Lett.* **99**, 192103 (2011).
- [142] S. E. Boulfelfel, G. Seifert, and S. Leoni, Atomistic investigation of Li⁺ diffusion pathways in the olivine LiFePO₄ cathode material, *J. Mater. Chem.* **21**, 16365 (2011).
- [143] W. C. Chueh *et al.*, Intercalation pathway in many-particle LiFePO₄ electrode revealed by nanoscale state-of-charge mapping, *Nano Lett.* **13**, 866 (2013).
- [144] P. Gibot, M. Casas-Cabanas, L. Laffont, S. Levasseur, P. Carlach, S. Hamelet, J.-M. Tarascon, and C. Masquelier, Room-temperature single-phase Li insertion/extraction in nanoscale Li_xFePO₄, *Nat. Mater.* **7**, 741 (2008).
- [145] C. Delmas, M. Maccario, L. Croguennec, F. Le Cras, and F. Weill, Lithium deintercalation in LiFePO₄ nanoparticles via a domino-cascade model, *Nat. Mater.* **7**, 665 (2008).
- [146] B. Ellis, L. K. Perry, D. H. Ryan, and L. F. Nazar, Small polaron hopping in Li_xFePO₄ solid solutions: Coupled lithium-ion and electron mobility, *J. Am. Chem. Soc.* **128**, 11416 (2006).
- [147] R. Amin, J. Maier, P. Balaya, D. P. Chen, and C. T. Lin, Ionic and electronic transport in single crystalline LiFePO₄

- grown by optical floating zone technique, *Solid-State Ionics* **179**, 1683 (2008).
- [148] L. Laffont *et al.*, Study of the $\text{LiFePO}_4/\text{FePO}_4$ two-phase system by high-resolution electron energy loss spectroscopy, *Chem. Mater.* **18**, 5520 (2006).
- [149] W. Sigle, R. Amin, K. Weichert, P. A. van Aken, and J. Maier, Delithiation study of LiFePO_4 crystals using electron energy-loss spectroscopy, *Electrochem. Solid-State Lett.* **12**, A151 (2009).
- [150] K. Weichert, W. Sigle, P. A. van Aken, J. Jamnik, C. Zhu, R. Amin, T. Acartürk, U. Starke, and J. Maier, Phase boundary propagation in large LiFePO_4 single crystals on delithiation, *J. Am. Chem. Soc.* **134**, 2988 (2012).
- [151] L. Gu, C. Zhu, H. Li, Y. Yu, C. Li, S. Tsukimoto, J. Maier, and Y. Ikuhara, Direct observation of lithium staging in partially delithiated LiFePO_4 at atomic resolution, *J. Am. Chem. Soc.* **133**, 4661 (2011).
- [152] N. Ohmer, B. Fenk, D. Samuelis, C.-C. Chen, J. Maier, M. Weigand, E. Goering, and G. Schütz, Phase evolution in single-crystalline LiFePO_4 followed by in situ scanning x-ray microscopy of a micrometre-sized battery, *Nat. Commun.* **6**, 6045 (2015).
- [153] C. Delacourt, P. Poizot, J.-M. Tarascon, and C. Masquelier, The existence of a temperature-driven solid solution in LiFePO_4 for $0 \leq x \leq 1$, *Nat. Mater.* **4**, 254 (2005).
- [154] D. A. Cogswell and M. Z. Bazant, Coherency strain and the kinetics of phase separation in LiFePO_4 nanoparticles, *ACS Nano* **6**, 2215 (2012).
- [155] M. Wagemaker, F. M. Mulder, and A. Van der Ven, The role of surface and interface energy on phase stability of nanosized insertion compounds, *Adv. Mater.* **21**, 2703 (2009).
- [156] M. J. Welland, D. Karpeyev, D. T. O'Connor, and O. Heinonen, Miscibility gap closure, interface morphology, and phase microstructure of 3D LiFePO_4 nanoparticles from surface wetting and coherency strain, *ACS Nano* **9**, 9757 (2015).
- [157] A. Jena and B. R. K. Nanda, Unconventional magnetism and band gap formation in LiFePO_4 : Consequences of polyanion induced non-planarity, *Sci. Rep.* **6**, 19573 (2016).
- [158] V. Singh, Y. Gershinshy, M. Kosa, M. Dixit, D. Zitoun, and D. T. Major, Magnetism in olivine-type $\text{LiCo}_{1-x}\text{Fe}_x\text{PO}_4$ cathode material: Bridging theory and experiments, *Phys. Chem. Chem. Phys.* **17**, 31202 (2015).
- [159] C. M. Julien, A. Ait-Salah, A. Mauger, and F. Gendron, Magnetic properties of lithium intercalation compounds, *Ionics* **12**, 21 (2006).
- [160] G. Rousse, J. Rodriguez-Carvajal, S. Patoux, and C. Masquelier, Magnetic structures of the triphylite LiFePO_4 and of its delithiated form FePO_4 , *Chem. Mater.* **15**, 4082 (2003).
- [161] P. H. L. Sit, R. Car, M. H. Cohen, and A. Selloni, Simple, unambiguous theoretical approach to oxidation state determination via first-principles calculations, *Inorgan. Chem.* **50**, 10259 (2011).
- [162] Oxidation state changes and electron flow in enzymatic catalysis and electrocatalysis through Wannier-function analysis.
- [163] G. Chen and T. J. Richardson, Thermal instability of olivine-type LiMnPO_4 cathodes, *J. Power Sources* **195**, 1221 (2010).
- [164] V. Aravindan, J. Gnanaraj, Y.-S. Lee, and S. Madhavi, LiMnPO_4 —A next generation cathode material for lithium-ion batteries, *J. Mater. Chem. A* **1**, 3518 (2013).
- [165] J. O. Herrera, H. Comancho-Montes, L. E. Fuentes, and L. Álvarez-Contreras, LiMnPO_4 review on synthesis and electrochemical properties, *J. Mater. Sci. Chem. Eng.* **3**, 54 (2015).
- [166] Z. X. Nie, C. Y. Ouyang, J. Z. Chen, Z. Y. Zhong, Y. L. Du, D. S. Liu, S. Q. Shi, and M. S. Lei, First principles study of Jahn-Teller effects in Li_xMnPO_4 , *Solid State Commun.* **150**, 40 (2010).
- [167] D. Choi, D. Wang, I.-T. Bae, J. Xiao, Z. Nie, W. Wang, G. L. Graff, Z. Yang, and J. Liu, LiMnPO_4 nanoplate grown via solid-state reaction in molten hydrocarbon for Li-ion battery cathode, *Nano Lett.* **10**, 2799 (2010).
- [168] J. Hong, F. Wang, X. Wang, and J. Graetz, $\text{LiFe}_x\text{Mn}_{1-x}\text{PO}_4$: A cathode for lithium-ion batteries, *J. Power Sources* **196**, 3659 (2011).
- [169] K. Zaghbi, M. Trudeau, A. Guerfi, J. Trottier, A. Mauger, R. Veillette, and C. M. Julien, New advanced cathode material: LiMnPO_4 encapsulated with LiFePO_4 , *J. Power Sources* **204**, 177 (2012).
- [170] A. Yamada, Y. Takei, H. Koizumi, N. Sonoyama, and R. Kanno, Electrochemical, magnetic, and structural investigation of the $\text{Li}_x(\text{Mn}_y\text{Fe}_{1-y})\text{PO}_4$ olivine phases, *Chem. Mater.* **18**, 804 (2006).
- [171] S. K. Martha, B. Markovsky, J. Grinblat, Y. Gofer, O. Haik, E. Zinigrad, D. Aurbach, T. Drenzen, D. Wang, G. Deghenghi, and I. Exnar, LiMnPO_4 as an advanced cathode material for rechargeable lithium batteries, *J. Electrochem. Soc.* **156**, A541 (2009).
- [172] M. Pivko, M. Bele, E. Tchernychova, N. Z. Logar, R. Dominko, and M. Gaberscek, Synthesis of nanometric LiMnPO_4 via a two-step technique, *Chem. Mater.* **24**, 1041 (2012).
- [173] Z. Bakenov and I. Taniguchi, LiMnPO_4 as a cathode for lithium batteries, *Open Mater. Sci. J.* **5**, 222 (2011).
- [174] G. Li, H. Azuma, and M. Tohda, LiMnPO_4 as the cathode for lithium batteries, *Electrochem. Solid-State Lett.* **5**, A135 (2002).
- [175] J. Xiao, W. Xu, D. Choi, and J.-G. Zhang, Synthesis and characterization of lithium manganese phosphate by a precipitation method, *J. Electrochem. Soc.* **157**, A142 (2010).
- [176] P. Goyal, M. K. Gupta, R. Mittal, S. Rols, S. J. Patwe, S. N. Achary, A. K. Tyagi, and S. L. Chaplot, Phonons, lithium diffusion and thermodynamics of LiMPO_4 ($M = \text{Mn, Fe}$), *J. Mater. Chem. A* **2**, 14729 (2014).
- [177] L. F. J. Piper, N. F. Quackenbush, S. Sallis, D. O. Scanlon, G. W. Watson, K.-W. Nam, X.-Q. Yang, K. E. Smith, F. Omenya, N. A. Chernova, and M. S. Whittingham, Elucidating the nature of pseudo Jahn-Teller distortions in LiMnPO_4 : Combining density functional theory with soft and hard x-ray spectroscopy, *J. Phys. Chem. C* **117**, 10383 (2013).
- [178] Y. Huang *et al.*, Understanding the stability of MnPO_4 , *J. Mater. Chem. A* **2**, 12827 (2014).
- [179] F. Zhou, K. Kang, T. Maxisch, G. Ceder, and D. Morgan, The electronic structure and band gap of LiFePO_4 and LiMnPO_4 , *Solid State Commun.* **132**, 181 (2004).
- [180] D. Morgan, A. Van der Ven, and G. Ceder, Li Conductivity in Li_xMPO_4 ($M = \text{Mn, Fe, Co, Ni}$) Olivine Materials, *Electrochem. Solid-State Lett.* **7**, A30 (2004).
- [181] K. Momma and F. Izumi, VESTA 3 for three-dimensional visualization of crystal, volumetric and morphology data, *J. Appl. Crystallogr.* **44**, 1272 (2011).